

This document has been superseded
by a later version. For the latest
version go to the web site:

<http://fire.nist.gov/fds>

Fire Dynamics Simulator (Version 3) – Technical Reference Guide

Kevin B. McGrattan
Howard R. Baum
Ronald G. Rehm
Anthony Hamins
Glenn P. Forney
Jason E. Floyd
Simo Hostikka
Kuldeep Prasad

NISTIR 6783, 2002 Ed.

Fire Dynamics Simulator (Version 3) – Technical Reference Guide

Kevin B. McGrattan
Howard R. Baum
Ronald G. Rehm
Anthony Hamins
Glenn P. Forney
Kuldeep Prasad
*Fire Research Division
Building and Fire Research Laboratory*

Jason E. Floyd
*Hughes Associates, Inc.
Baltimore, Maryland*

Simo Hostikka
*VTT Building and Transport
Finland*

November 2002



U.S. Department of Commerce
Donald L. Evans, Secretary

National Institute of Standards and Technology
Arden L. Bement, Director

Disclaimer

The US Department of Commerce makes no warranty, expressed or implied, to users of the Fire Dynamics Simulator (FDS), and accepts no responsibility for its use. Users of FDS assume sole responsibility under Federal law for determining the appropriateness of its use in any particular application; for any conclusions drawn from the results of its use; and for any actions taken or not taken as a result of analyses performed using these tools.

Users are warned that FDS is intended for use only by those competent in the fields of fluid dynamics, thermodynamics, combustion, and heat transfer, and is intended only to supplement the informed judgment of the qualified user. The software package is a computer model that may or may not have predictive capability when applied to a specific set of factual circumstances. Lack of accurate predictions by the model could lead to erroneous conclusions with regard to fire safety. All results should be evaluated by an informed user.

Throughout this document, the mention of computer hardware or commercial software does not constitute endorsement by NIST, nor does it indicate that the products are necessarily those best suited for the intended purpose.

Contents

1	Introduction	1
2	Hydrodynamic Model	3
2.1	Conservation Equations	3
2.2	State, Mass and Energy Equations	3
2.3	The Momentum Equation	5
2.4	Diffusive Terms (LES)	6
2.5	Diffusive Terms (DNS)	7
3	Combustion	8
3.1	Mixture Fraction Combustion Model	8
3.2	Enhancements to the Mixture Fraction Model	10
3.3	Finite-rate Reaction (DNS)	11
4	Thermal Radiation	13
5	Thermal Boundary Conditions	16
5.1	Convective Heat Transfer to Walls	16
5.2	Pyrolysis Model, Thermally-Thick Solid	16
5.3	Pyrolysis Model, Thermally-Thin Solid	17
5.4	Pyrolysis Model, Liquid Fuels	17
6	Sprinklers	19
6.1	Sprinkler Activation	19
6.2	Sprinkler Droplet Size Distribution	19
6.3	Sprinkler Droplet Trajectory in Air	21
6.4	Sprinkler Droplet Transport on a Surface	21
6.5	Mass and Energy Transfer from Droplets	21
6.6	Interaction of Droplets and Radiation	22
6.7	Fire Suppression by Water	23
7	Numerical Method	25
7.1	Simplified Equations	25
7.2	Temporal Discretization	25
7.3	Spatial Discretization	26
7.4	Large Eddy vs. Direct Numerical Simulation	27
7.5	The Mass Transport Equations	28
7.5.1	Convective and Diffusive Transport	28
7.6	Discretizing the Divergence	29
7.6.1	Heat Release Rate (Mixture Fraction)	29
7.6.2	Heat Release Rate (Finite-Rate Reaction)	30
7.7	Thermal Radiation	31
7.8	Interaction of Droplets and Radiation	34
7.9	Thermal and Material Boundary Conditions	34
7.10	The Momentum Equation	37
7.10.1	Force Terms	38
7.10.2	Time Step	39

7.11 The Pressure Equation	39
7.12 Particle Tracking	40
8 Conclusion	41
9 Nomenclature	42
References	44

1 Introduction

The idea that the dynamics of a fire might be studied numerically dates back to the beginning of the computer age. Indeed, the fundamental conservation equations governing fluid dynamics, heat transfer, and combustion were first written down over a century ago. Despite this, practical mathematical models of fire (as distinct from controlled combustion) are relatively recent due to the inherent complexity of the problem. Indeed, in his brief history of the early days of fire research, Hoyt Hottel noted “A case can be made for fire being, next to the life processes, the most complex of phenomena to understand” [1].

The difficulties revolve about three issues: First, there are an enormous number of possible fire scenarios to consider due to their accidental nature. Second, the physical insight and computing power necessary to perform all the necessary calculations for most fire scenarios are limited. Any fundamentally based study of fires must consider at least some aspects of bluff body aerodynamics, multi-phase flow, turbulent mixing and combustion, radiative transport, and conjugate heat transfer; all of which are active research areas in their own right. Finally, the “fuel” in most fires was never intended as such. Thus, the mathematical models and the data needed to characterize the degradation of the condensed phase materials that supply the fuel may not be available. Indeed, the mathematical modeling of the physical and chemical transformations of real materials as they burn is still in its infancy.

In order to make progress, the questions that are asked have to be greatly simplified. To begin with, instead of seeking a methodology that can be applied to all fire problems, we begin by looking at a few scenarios that seem to be most amenable to analysis. Hopefully, the methods developed to study these “simple” problems can be generalized over time so that more complex scenarios can be analyzed. Second, we must learn to live with idealized descriptions of fires and approximate solutions to our idealized equations. Finally, the methods should be capable of systematic improvement. As our physical insight and computing power grow more powerful, the methods of analysis can grow with them.

To date, three distinct approaches to the simulation of fires have emerged. Each of these treats the fire as an inherently three dimensional process evolving in time. The first to reach maturity, the “zone” models, describe compartment fires. Each compartment is divided into two spatially homogeneous volumes, a hot upper layer and a cool lower layer. Mass and energy balances are enforced for each layer, with additional models describing other physical processes appended as differential or algebraic equations as appropriate. Examples of such phenomena include fire plumes, flows through doors, windows and other vents, radiative and convective heat transfer, and solid fuel pyrolysis. An excellent description of the physical and mathematical assumptions behind the zone modeling concept is given by Quintiere [2], who chronicles developments through 1983. Model development since then has progressed to the point where documented and supported software implementing these models are widely available [3].

The relative physical and computational simplicity of the zone models has led to their widespread use in the analysis of fire scenarios. So long as detailed spatial distributions of physical properties are not required, and the two layer description reasonably approximates reality, these models are quite reliable. However, by their very nature, there is no way to systematically improve them. The rapid growth of computing power and the corresponding maturing of computational fluid dynamics (CFD), has led to the development of CFD based “field” models applied to fire research problems. Virtually all this work is based on the conceptual framework provided by the Reynolds-averaged form of the governing equations, in particular the $k - \epsilon$ turbulence model pioneered by Patankar and Spalding [4]. The use of CFD models has allowed the description of fires in complex geometries, and the incorporation of a wide variety of physical phenomena. However, these models have a fundamental limitation for fire applications – the averaging procedure at the root of the model equations. The $k - \epsilon$ model was developed as a time-averaged approximation to the conservation equations of fluid dynamics. While the precise nature of the averaging time is not specified, it is clearly long enough to require the introduction of large eddy transport coefficients to describe the unresolved fluxes of mass, momentum and energy. This is the root cause of the smoothed appearance of the results of

even the most highly resolved fire simulations. The smallest resolvable length scales are determined by the product of the local velocity and the averaging time, rather than the spatial resolution of the underlying computational grid. This property of the $k - \epsilon$ model is typically exploited in numerical computations by using implicit numerical techniques to take large time steps.

Unfortunately, the evolution of large eddy structures characteristic of most fire plumes is lost with such an approach, as is the prediction of local transient events. It is sometimes argued that the averaging process used to define the equations is an “ensemble average” over many replicates of the same experiment or postulated scenario. However, this is a moot point in fire research since neither experiments nor real scenarios are replicated in the sense required by that interpretation of the equations. The application of “Large Eddy Simulation” (LES) techniques to fire is aimed at extracting greater temporal and spatial fidelity from simulations of fire performed on the more finely meshed grids allowed by ever faster computers. The phrase LES refers to the description of turbulent mixing of the gaseous fuel and combustion products with the local atmosphere surrounding the fire. This process, which determines the burning rate in most fires and controls the spread of smoke and hot gases, is extremely difficult to predict accurately. This is true not only in fire research but in almost all phenomena involving turbulent fluid motion. The basic idea behind the LES technique is that the eddies that account for most of the mixing are large enough to be calculated with reasonable accuracy from the equations of fluid dynamics. The hope (which must ultimately be justified by appeal to experiments) is that small-scale eddy motion can either be crudely accounted for or ignored.

The equations describing the transport of mass, momentum, and energy by the fire induced flows must be simplified so that they can be efficiently solved for the fire scenarios of interest. The general equations of fluid dynamics describe a rich variety of physical processes, many of which have nothing to do with fires. Retaining this generality would lead to an enormously complex computational task that would shed very little additional insight on fire dynamics. The simplified equations, developed by Rehm and Baum [5], have been widely adopted by the larger combustion research community, where they are referred to as the “low Mach number” combustion equations. They describe the low speed motion of a gas driven by chemical heat release and buoyancy forces.

The low Mach number equations are solved numerically by dividing the physical space where the fire is to be simulated into a large number of rectangular cells. Within each cell the gas velocity, temperature, *etc.*, are assumed to be uniform; changing only with time. The accuracy with which the fire dynamics can be simulated depends on the number of cells that can be incorporated into the simulation. This number is ultimately limited by the computing power available. Present day desktop computers limit the number of such cells to at most a few million. This means that the ratio of largest to smallest eddy length scales that can be resolved by the computation (the “dynamic range” of the simulation) is roughly $100 \sim 200$. Unfortunately, the range of length scales that need to be accounted for if all relevant fire processes are to be simulated is roughly $10^4 \sim 10^5$ because combustion processes take place at length scales of 1 mm or less, while the length scales associated with building fires are of the order of meters or tens of meters. The form of the numerical equations discussed below depends on which end of the spectrum one wants to capture directly, and which end is to be ignored or approximated.

2 Hydrodynamic Model

An approximate form of the Navier-Stokes equations appropriate for low Mach number applications is used in the model. The approximation involves the filtering out of acoustic waves while allowing for large variations in temperature and density [5]. This gives the equations an elliptic character, consistent with low speed, thermal convective processes. The computation can either be treated as a Direct Numerical Simulation (DNS), in which the dissipative terms are computed directly, or as a Large Eddy Simulation (LES), in which the large-scale eddies are computed directly and the sub-grid scale dissipative processes are modeled. The choice of DNS vs. LES depends on the objective of the calculation and the resolution of the computational grid. If, for example, the problem is to simulate the flow of smoke through a large, multi-room enclosure, it is not possible to resolve the combustion and transport processes directly. However, for small-scale combustion experiments, it is possible to compute the transport directly and the combustion processes to some extent.

2.1 Conservation Equations

First, consider the conservation equations of mass, momentum and energy for a thermally-expandable, multi-component mixture of ideal gases [5]:

Conservation of Mass

$$\frac{\partial \rho}{\partial t} + \nabla \cdot \rho \mathbf{u} = 0 \quad (1)$$

Conservation of Species

$$\frac{\partial}{\partial t}(\rho Y_l) + \nabla \cdot \rho Y_l \mathbf{u} = \nabla \cdot \rho D_l \nabla Y_l + \dot{m}_l''' \quad (2)$$

Conservation of Momentum

$$\rho \left(\frac{\partial \mathbf{u}}{\partial t} + (\mathbf{u} \cdot \nabla) \mathbf{u} \right) + \nabla p = \rho \mathbf{g} + \mathbf{f} + \nabla \cdot \boldsymbol{\tau} \quad (3)$$

Conservation of Energy

$$\frac{\partial}{\partial t}(\rho h) + \nabla \cdot \rho h \mathbf{u} = \frac{Dp}{Dt} - \nabla \cdot \mathbf{q}_r + \nabla \cdot k \nabla T + \sum_l \nabla \cdot h_l \rho D_l \nabla Y_l \quad (4)$$

Note that the external force on the fluid, represented by the term \mathbf{f} in Eq. (3), consists of the drag exerted by water droplets emanating from sprinklers plus other external forces. The term $Dp/Dt = \partial p/\partial t + \mathbf{u} \cdot \nabla p$ is a material derivative. All other symbols are listed in the Nomenclature (Section 9).

2.2 State, Mass and Energy Equations

The conservation equations are supplemented by an equation of state relating the thermodynamic quantities. An approximation to the ideal gas law is made by decomposing the pressure into a “background” component, a hydrostatic component, and a flow-induced perturbation

$$p = p_0 - \rho_\infty g z + \tilde{p} \quad (5)$$

For most applications, p_0 is constant and the other two components are relatively small. Adjustments to this assumption can be made in the case when the pressure rises due to a fire in a tightly sealed enclosure, or

when the height of the domain is on the order of a kilometer and p_0 can no longer be assumed constant and must be considered a function of the altitude [6].

The purpose of decomposing the pressure is that for low-Mach number flows, it can be assumed that the temperature and density are inversely proportional, and thus the equation of state can be approximated [5]

$$p_0 = \rho T \mathcal{R} \sum (Y_i/M_i) = \rho T \mathcal{R}/M \quad (6)$$

The pressure p in the state and energy equations is replaced by the background pressure p_0 to filter out sound waves that travel at speeds that are much faster than typical flow speeds expected in fire applications. The low Mach number assumption serves two purposes. First, the filtering of acoustic waves means that the time step in the numerical algorithm is bound only by the flow speed as opposed to the speed of sound, and second, the modified state equation leads to a reduction in the number of dependent variables in the system of equations by one. The energy equation (4) is never explicitly solved, but its source terms are included in the expression for the flow divergence, an important quantity in the analysis to follow.

The divergence of the flow is obtained by taking the material derivative of the equation of state, and then substituting terms from the mass and energy conservation equations. First, define the constant-pressure specific heat of the mixture: $c_p = \sum_l c_{p,l} Y_l$ where $c_{p,l}$ is the temperature-dependent specific heat of species l . Next, define the enthalpy $h = \sum_l h_l Y_l$ where

$$h_l(T) = h_l^0 + \int_{T^0}^T c_{p,l}(T') dT' \quad (7)$$

and h_l^0 is the heat of formation of species l . Now the divergence can be written

$$\begin{aligned} \nabla \cdot \mathbf{u} = & \frac{1}{\rho c_p T} \left(\nabla \cdot k \nabla T + \nabla \cdot \sum_l \int c_{p,l} dT \rho D_l \nabla Y_l - \nabla \cdot \mathbf{q}_r \right) + \\ & \frac{M}{\rho} \sum_l \nabla \cdot \rho D_l \nabla (Y_l/M_l) - \frac{1}{\rho c_p T} \sum_l \int c_{p,l} dT \nabla \cdot \rho D_l \nabla Y_l + \\ & \frac{1}{\rho} \sum_l \left(\frac{M}{M_l} - \frac{h_l}{c_p T} \right) \dot{m}_l''' + \left(\frac{1}{\rho c_p T} - \frac{1}{p_0} \right) \frac{dp_0}{dt} \end{aligned} \quad (8)$$

This expression can be simplified by making some approximations. First, assume that $\int c_{p,l} dT \approx c_{p,l} T$. Further, assume the specific heat can be expressed in terms of the number of internal degrees of freedom ν_l active in the molecule.

$$c_{p,l} = \left(\frac{2 + \nu_l}{2} \right) \frac{\mathcal{R}}{M_l} = \left(\frac{\gamma_l}{\gamma_l - 1} \right) \frac{\mathcal{R}}{M_l} \quad (9)$$

If the ratio of specific heats γ_l for each species is assumed to be constant, the second line of Eq. (8) disappears, and the only term left from the production term in line 3 is

$$\frac{1}{\rho} \sum_l \left(\frac{M}{M_l} - \frac{h_l}{c_p T} \right) \dot{m}_l''' = -\frac{1}{\rho c_p T} \sum_l h_l^0 \dot{m}_l''' \quad (10)$$

which can be regarded as the energy due to the reaction. From here on, the reaction energy release rate per unit volume will be written $\dot{q}''' = -\sum_l h_l^0 \dot{m}_l'''$.

The approximate form of the divergence used in the calculation is

$$\nabla \cdot \mathbf{u} = \frac{1}{\rho c_p T} \left(\nabla \cdot k \nabla T + \nabla \cdot \sum_l \int c_{p,l} dT \rho D_l \nabla Y_l - \nabla \cdot \mathbf{q}_r + \dot{q}''' \right) + \left(\frac{1}{\rho c_p T} - \frac{1}{p_0} \right) \frac{dp_0}{dt} \quad (11)$$

Notice that the assumption of a temperature-independent specific heat was made only to eliminate minor terms in the divergence expression, and thereby reduce the cost of the calculation. In general, it is not assumed that the specific heat is independent of temperature. The pressure rise term on the right hand side of the divergence expression is non-zero only if it assumed that the enclosure is tightly sealed, in which case the background pressure p_0 can no longer be assumed constant due to the increase (or decrease) in mass and thermal energy within the enclosure. The evolution equation for the pressure is found by integrating Eq. (11) over the entire domain Ω

$$\frac{dp_0}{dt} = \left[\int_{\Omega} \frac{1}{\rho c_p T} (\nabla \cdot k \nabla T + \dots) dV - \int_{\partial\Omega} \mathbf{u} \cdot d\mathbf{S} \right] / \int_{\Omega} \left(\frac{1}{p_0} - \frac{1}{\rho c_p T} \right) dV \quad (12)$$

2.3 The Momentum Equation

The momentum equation is simplified by subtracting off the hydrostatic pressure gradient from the momentum equation (3), and then dividing by the density to obtain¹

$$\frac{\partial \mathbf{u}}{\partial t} - \mathbf{u} \times \boldsymbol{\omega} + \frac{1}{2} \nabla |\mathbf{u}|^2 + \frac{1}{\rho} \nabla \tilde{p} = \frac{1}{\rho} ((\rho - \rho_{\infty}) \mathbf{g} + \mathbf{f} + \nabla \cdot \boldsymbol{\tau}) \quad (13)$$

To simplify this equation further, a substitution is made

$$\nabla \mathcal{H} \approx \frac{1}{2} \nabla |\mathbf{u}|^2 + \frac{1}{\rho} \nabla \tilde{p} \quad (14)$$

The basis for this approximation is seen in the evolution equation for the circulation, obtained by integrating Eq. (13) over a closed loop moving with the fluid (in the absence of any external force)

$$\frac{d\Gamma}{dt} = \oint \frac{1}{\rho} (-\nabla \tilde{p} + (\rho - \rho_{\infty}) \mathbf{g} + \nabla \cdot \boldsymbol{\tau}) \cdot d\mathbf{x} \quad (15)$$

There are three sources of vorticity: the baroclinic torque due to the non-alignment of the density and pressure gradients, buoyancy due to horizontal density gradients, and viscosity. Buoyancy is the dominant source of vorticity, and the approximation above is equivalent to neglecting the baroclinic torque.²

Neglecting the baroclinic torque simplifies the elliptic partial differential equation obtained by taking the divergence of the momentum equation

$$\nabla^2 \mathcal{H} = -\frac{\partial(\nabla \cdot \mathbf{u})}{\partial t} - \nabla \cdot \mathbf{F} \quad ; \quad \mathbf{F} = -\mathbf{u} \times \boldsymbol{\omega} - \frac{1}{\rho} ((\rho - \rho_{\infty}) \mathbf{g} + \mathbf{f} + \nabla \cdot \boldsymbol{\tau}) \quad (16)$$

The linear algebraic system arising from the discretization of Eq. (16) has constant coefficients and can be solved to machine accuracy by a fast, direct (*i.e.* non-iterative) method that utilizes fast Fourier transforms. No-flux or forced-flow boundary conditions are specified by asserting that

$$\frac{\partial \mathcal{H}}{\partial n} = -F_n - \frac{\partial u_n}{\partial t} \quad (17)$$

¹Note the use of the vector identity $(\mathbf{u} \cdot \nabla) \mathbf{u} = \frac{1}{2} \nabla |\mathbf{u}|^2 - \mathbf{u} \times \boldsymbol{\omega}$.

²An option exists in the code to restore the baroclinic torque by decomposing the pressure term

$$\frac{\nabla \tilde{p}}{\rho} = \frac{\nabla \tilde{p}}{\bar{\rho}} + \left(\frac{1}{\rho} - \frac{1}{\bar{\rho}} \right) \nabla \tilde{p}$$

and evaluating the second term on the right hand side at the previous time step. The expression $\bar{\rho}$ is an average density, equal to $2\rho_{\min}\rho_{\max}/(\rho_{\min} + \rho_{\max})$. For most large-scale applications, the baroclinic torque is relatively small compared to buoyancy.

where F_n is the normal component of \mathbf{F} at the vent or solid wall, and $\partial u_n / \partial t$ is the prescribed rate of change in the normal component of velocity at a forced vent. Initially, the velocity is zero everywhere. At open external boundaries the pressure-like term \mathcal{H} is prescribed, depending on whether the flow is outgoing or incoming

$$\begin{aligned} \mathcal{H} &= |\mathbf{u}|^2/2 && \text{outgoing} \\ \mathcal{H} &= 0 && \text{incoming} \end{aligned} \quad (18)$$

The outgoing boundary condition assumes that the pressure perturbation \tilde{p} is zero at an outgoing boundary and that \mathcal{H} is constant along streamlines. The incoming boundary condition assumes that \mathcal{H} is zero infinitely far away.

2.4 Diffusive Terms (LES)

The viscous stress tensor in the momentum equation is given by

$$\boldsymbol{\tau} = \mu \left(2 \text{def } \mathbf{u} - \frac{2}{3} (\nabla \cdot \mathbf{u}) \mathbf{I} \right) \quad (19)$$

where \mathbf{I} is the identity matrix and the deformation tensor is defined

$$\text{def } \mathbf{u} \equiv \frac{1}{2} [\nabla \mathbf{u} + (\nabla \mathbf{u})^t] = \begin{pmatrix} \frac{\partial u}{\partial x} & \frac{1}{2} \left(\frac{\partial u}{\partial y} + \frac{\partial v}{\partial x} \right) & \frac{1}{2} \left(\frac{\partial u}{\partial z} + \frac{\partial w}{\partial x} \right) \\ \frac{1}{2} \left(\frac{\partial v}{\partial x} + \frac{\partial u}{\partial y} \right) & \frac{\partial v}{\partial y} & \frac{1}{2} \left(\frac{\partial v}{\partial z} + \frac{\partial w}{\partial y} \right) \\ \frac{1}{2} \left(\frac{\partial w}{\partial x} + \frac{\partial u}{\partial z} \right) & \frac{1}{2} \left(\frac{\partial w}{\partial y} + \frac{\partial v}{\partial z} \right) & \frac{\partial w}{\partial z} \end{pmatrix} \quad (20)$$

In the numerical model, there are two options for treating the dynamic viscosity μ . For a Large Eddy Simulation (LES) where the grid resolution is not fine enough to capture the mixing processes at all relevant scales, a sub-grid scale model for the viscosity is applied. Following the analysis of Smagorinsky [7], the viscosity can be modeled as

$$\mu_{\text{LES}} = \rho (C_s \Delta)^2 \left(2(\text{def } \mathbf{u}) \cdot (\text{def } \mathbf{u}) - \frac{2}{3} (\nabla \cdot \mathbf{u})^2 \right)^{\frac{1}{2}} \quad (21)$$

where C_s is an empirical constant, Δ is a length on the order of the size of a grid cell, and the deformation term is related to the Dissipation Function

$$\Phi \equiv \boldsymbol{\tau} \cdot \nabla \mathbf{u} \equiv \mu \left(2(\text{def } \mathbf{u}) \cdot (\text{def } \mathbf{u}) - \frac{2}{3} (\nabla \cdot \mathbf{u})^2 \right) \quad (22)$$

$$= \mu \left[2 \left(\frac{\partial u}{\partial x} \right)^2 + 2 \left(\frac{\partial v}{\partial y} \right)^2 + 2 \left(\frac{\partial w}{\partial z} \right)^2 + \right. \quad (23)$$

$$\left. \left(\frac{\partial v}{\partial x} + \frac{\partial u}{\partial y} \right)^2 + \left(\frac{\partial w}{\partial y} + \frac{\partial v}{\partial z} \right)^2 + \left(\frac{\partial u}{\partial z} + \frac{\partial w}{\partial x} \right)^2 - \frac{2}{3} \left(\frac{\partial u}{\partial x} + \frac{\partial v}{\partial y} + \frac{\partial w}{\partial z} \right)^2 \right] \quad (24)$$

The dissipation function is the rate at which kinetic energy is transferred to thermal energy. It is a source term in the energy conservation equation that is usually neglected because it is small – an approximation consistent with the low Mach number equations.

In an LES calculation, the thermal conductivity and material diffusivity are related to the turbulent viscosity by

$$k_{\text{LES}} = \frac{\mu_{\text{LES}} c_p}{\text{Pr}} \quad ; \quad (\rho D)_{l,\text{LES}} = \frac{\mu_{\text{LES}}}{\text{Sc}} \quad (25)$$

The Prandtl number Pr and the Schmidt number Sc are assumed to be constant for a given scenario.

There have been numerous refinements of the original Smagorinsky model [8, 9, 10], but it is difficult to assess the improvements offered by these newer schemes. There are two reasons for this. First, the structure of the fire plume is so dominated by the large-scale resolvable eddies that even a constant eddy viscosity gives results almost identical to those obtained using the Smagorinsky model [11]. Second, the lack of precision in most large-scale fire test data makes it difficult to assess the relative accuracy of each model. The Smagorinsky model with constant C_s produces satisfactory results for most large-scale applications where boundary layers are not well resolved.

2.5 Diffusive Terms (DNS)

For a Direct Numerical Simulation (DNS), the viscosity, thermal conductivity and material diffusivity are approximated from kinetic theory. The viscosity of the l th species is given by

$$\mu_l = \frac{26.69 \times 10^{-7} (M_l T)^{\frac{1}{2}}}{\sigma_l^2 \Omega_v} \quad \frac{\text{kg}}{\text{m s}} \quad (26)$$

where σ_l is the Lennard-Jones hard-sphere diameter (\AA) and Ω_v is the collision integral, an empirical function of the temperature T . The thermal conductivity of the l th species is given by

$$k_l = \frac{\mu_l c_{p,l}}{Pr} \quad \frac{\text{W}}{\text{m K}} \quad (27)$$

where the Prandtl number Pr is 0.7. The viscosity and thermal conductivity of a gas mixture are given by

$$\mu_{\text{DNS}} = \sum_l Y_l \mu_l \quad ; \quad k_{\text{DNS}} = \sum_l Y_l k_l \quad (28)$$

The binary diffusion coefficient of the l th species diffusing into the m th species is given by

$$D_{lm} = \frac{2.66 \times 10^{-7} T^{3/2}}{M_{lm}^{\frac{1}{2}} \sigma_{lm}^2 \Omega_D} \quad \frac{\text{m}^2}{\text{s}} \quad (29)$$

where $M_{lm} = 2(1/M_l + 1/M_m)^{-1}$, $\sigma_{lm} = (\sigma_l + \sigma_m)/2$, and Ω_D is the diffusion collision integral, an empirical function of the temperature T [12]. It is assumed that nitrogen is the dominant species in any combustion scenario considered here, thus the diffusion coefficient in the species mass conservation equations is that of the given species diffusing into nitrogen

$$(\rho D)_{l,\text{DNS}} = \rho D_{l0} \quad (30)$$

where species 0 is nitrogen.

3 Combustion

There are two types of combustion models used in FDS. The choice depends on the resolution of the underlying grid. For a DNS calculation where the diffusion of fuel and oxygen can be modeled directly, a global one-step, finite-rate chemical reaction is most appropriate. However, in an LES calculation where the grid is not fine enough to resolve the diffusion of fuel and oxygen, a mixture fraction-based combustion model is used.

3.1 Mixture Fraction Combustion Model

The mixture fraction combustion model is based on the assumption that large-scale convective and radiative transport phenomena can be simulated directly, but physical processes occurring at small length and time scales must be represented in an approximate manner. The nature of the approximations employed are necessarily a function of the spatial and temporal resolution limits of the computation, as well as our current (often limited) understanding of the phenomena involved.

The actual chemical rate processes that control the combustion energy release are often unknown in fire scenarios. Even if they were known, the spatial and temporal resolution limits imposed by both present and foreseeable computer resources places a detailed description of combustion processes beyond reach. Thus, the model adopted here is based on the assumption that the combustion is mixing-controlled. This implies that all species of interest can be described in terms of a mixture fraction $Z(\mathbf{x}, t)$. The mixture fraction is a conserved quantity representing the fraction of material at a given point that originated as fuel. The relations between the mass fraction of each species and the mixture fraction are known as “state relations”. The state relation for the oxygen mass fraction provides the information needed to calculate the local oxygen mass consumption rate. The form of the state relation that emerges from classical laminar diffusion flame theory is a piecewise linear function. This leads to a “flame sheet” model, where the flame is a two dimensional surface embedded in a three dimensional space. The local heat release rate is computed from the local oxygen consumption rate at the flame surface, assuming that the heat release rate is directly proportional to the oxygen consumption rate, independent of the fuel involved. This relation, originally proposed by Huggett [13], is the basis of oxygen calorimetry.

Start with the most general form of the combustion reaction



The numbers v_i are the stoichiometric coefficients for the overall combustion process that reacts fuel “F” with oxygen “O” to produce a number of products “P”. The stoichiometric equation (31) implies that the mass consumption rates for fuel and oxidizer are related as follows:

$$\frac{\dot{m}_F'''}{v_F M_F} = \frac{\dot{m}_O'''}{v_O M_O} \quad (32)$$

The mixture fraction Z is defined as:

$$Z = \frac{s Y_F - (Y_O - Y_O^\infty)}{s Y_F^I + Y_O^\infty} \quad ; \quad s = \frac{v_O M_O}{v_F M_F} \quad (33)$$

By design, it varies from $Z = 1$ in a region containing only fuel to $Z = 0$ where the oxygen mass fraction takes on its undepleted ambient value, Y_O^∞ . Note that Y_F^I is the fraction of fuel in the fuel stream. The quantities M_F and M_O are the fuel and oxygen molecular weights, respectively. The mixture fraction satisfies the conservation law

$$\rho \frac{DZ}{Dt} = \nabla \cdot \rho D \nabla Z \quad (34)$$

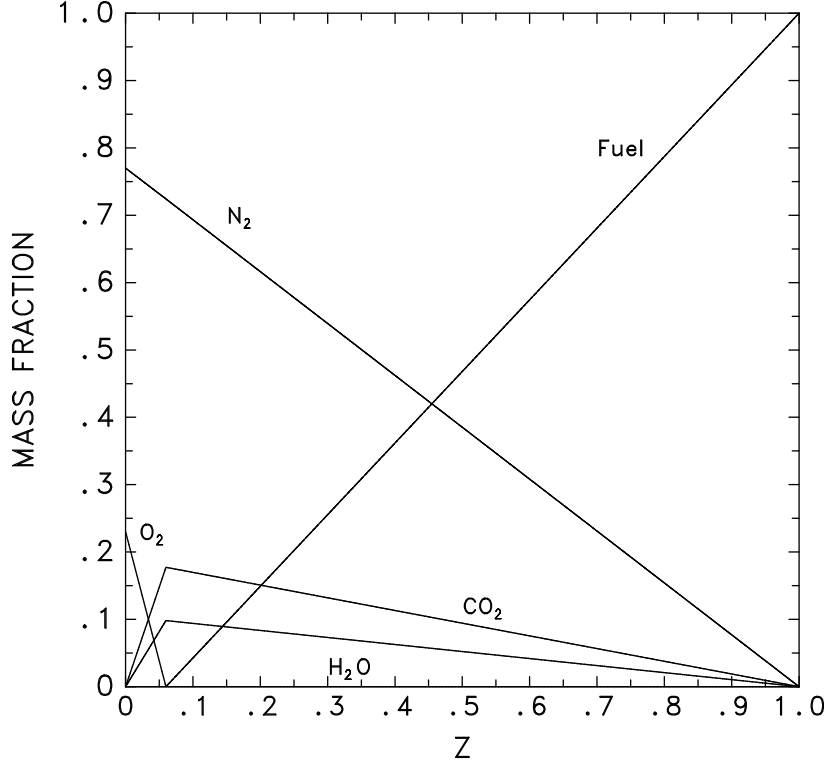


FIGURE 1: State relations for propane.

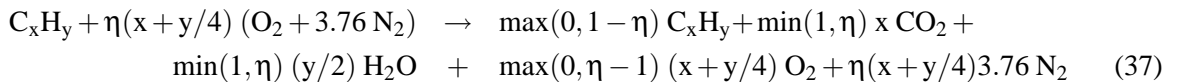
obtained from a linear combination of the fuel and oxygen conservation equations. The assumption that the chemistry is “fast” means that the reactions that consume fuel and oxidizer occur so rapidly that the fuel and oxidizer cannot co-exist. The requirement that fuel and oxidizer simultaneously vanish defines a flame surface as:

$$Z(\mathbf{x}, t) = Z_f \quad ; \quad Z_f = \frac{Y_O^\infty}{sY_F^I + Y_O^\infty} \quad (35)$$

The assumption that fuel and oxidizer cannot co-exist leads to the “state relation” between the oxygen mass fraction Y_O and Z

$$Y_O(Z) = \begin{cases} Y_O^\infty(1 - Z/Z_f) & Z < Z_f \\ 0 & Z > Z_f \end{cases} \quad (36)$$

State relations for both reactants and products can be derived by considering the following ideal reaction of a hydrocarbon fuel:



Here η is a parameter ranging from 0 (all fuel with no oxygen) to infinity (all oxygen with no fuel). A correspondence between η and Z is obtained by applying the definition of Z (Eq. 33) to the left hand side of Eq. (37). Mass fractions of the products of the infinitely fast reaction (including excess fuel or oxygen) can be obtained from the right hand side of Eq. (37). State relations for the ideal reaction of propane and air is shown in Fig. 1.

An expression for the local heat release rate can be derived from the conservation equations and the state relation for oxygen. The starting point is Huggett’s [13] relationship for the heat release rate as a function

of the oxygen consumption

$$\dot{q}''' = \Delta H_O \dot{m}_O''' \quad (38)$$

Here, ΔH_O is the heat release rate per unit mass of oxygen consumed. The oxygen mass conservation equation

$$\rho \frac{DY_O}{Dt} = \nabla \cdot \rho D \nabla Y_O + \dot{m}_O''' \quad (39)$$

can be transformed into an expression for the local heat release rate using the conservation equation for the mixture fraction (34) and the state relation for oxygen $Y_O(Z)$.

$$-\dot{m}_O''' = \nabla \cdot \left(\rho D \frac{dY_O}{dZ} \nabla Z \right) - \frac{dY_O}{dZ} \nabla \cdot \rho D \nabla Z = \rho D \frac{d^2 Y_O}{dZ^2} |\nabla Z|^2 \quad (40)$$

Neither of these expressions for the local oxygen consumption rate is particularly convenient to apply numerically because of the discontinuity of the derivative of $Y_O(Z)$ at $Z = Z_f$. However, an expression for the oxygen consumption rate per unit area of flame sheet can be derived from Eq. (40)

$$-\dot{m}_O'' = \left. \frac{dY_O}{dZ} \right|_{Z < Z_f} \rho D \nabla Z \cdot \mathbf{n} \quad (41)$$

In the numerical algorithm, the local heat release rate is computed by first locating the flame sheet, then computing the local heat release rate per unit area, and finally distributing this energy to the grid cells cut by the flame sheet. In this way, the ideal, infinitely thin flame sheet is smeared out over the width of a grid cell, consistent with all other gas phase quantities.

3.2 Enhancements to the Mixture Fraction Model

The mixture fraction model described in the previous section has several limitations, both numerical and physical. Its numerical limitations are related to the resolution of the underlying numerical grid. On coarse grids, the accuracy of the fuel transport and combustion processes is diminished by the high levels of numerical diffusion. The above procedure for determining the local heat release rate works well for calculations in which the fire is adequately resolved. A measure of how well the fire is resolved is given by the nondimensional expression $D^*/\delta x$, where D^* is a characteristic fire diameter

$$D^* = \left(\frac{\dot{Q}}{\rho_\infty c_p T_\infty \sqrt{g}} \right)^{5/3} \quad (42)$$

and δx is the nominal size of a grid cell³. The quantity $D^*/\delta x$ can be thought of as the number of computational cells spanning the characteristic (not necessarily the physical) diameter of the fire. The more cells spanning the fire, the better the resolution of the calculation. For fire scenarios where D^* is small relative to the physical diameter of the fire, and/or the numerical grid is relatively coarse, the stoichiometric surface $Z = Z_f$ will underestimate the observed flame height [14]. It has been found empirically that a good estimate of flame height can be found for crude grids if a different value of Z is used to define the combustion region

$$\frac{Z_{f,\text{eff}}}{Z_f} = \min \left(1, C \frac{D^*}{\delta x} \right) \quad (43)$$

Here C is an empirical constant to be used for all fire scenarios. As the resolution of the calculation increases, the $Z_{f,\text{eff}}$ approaches the ideal value, Z_f . The benefit of the expression is that it provides a quantifiable

³The characteristic fire diameter is related to the characteristic fire size via the relation $Q^* = (D^*/D)^{5/2}$, where D is the physical diameter of the fire.

measure of the grid resolution that takes into account not only the size of the grid cells, but also the size of the fire.

Another consequence of a coarse numerical grid is that a disproportionate amount of the combustion energy is released near the edges of the burner. From Eq. 41, it can be seen that the heat release rate per unit area of the flame sheet is proportional to the local gradient of the mixture fraction and the local value of the material diffusivity. The gradient of the mixture fraction is large at the base of the fire because there a stream of pure fuel meets surrounding air. The diffusivity is large on a coarse grid because it is related to the Smagorinsky viscosity. To prevent too much of the energy from being released too close to the burner when a coarse grid is used, there is a maximum bound imposed on the local heat release rate per unit area of flame sheet. This upper bound is based on an analysis in which the fire is assumed to be conical in shape with surface area, A , and a flame height, H , given by Heskestad's correlation [15]

$$H/D = 3.7 Q^{*2/5} - 1.02 \quad ; \quad A = \pi r \sqrt{r^2 + h^2} \quad (44)$$

The surface area of a real flame is larger than that of a cone, so the upper bound estimate will prevent too much energy from being released too close to the fire when a coarse grid is used, but will be high enough not to interfere with the calculation when the grid is well-resolved. Any energy that is “clipped” off due to the upper bound is redistributed over the entire flame volume.

The physical limitation of the mixture fraction approach is that it is assumed that fuel and oxygen burn instantaneously when mixed. For large-scale, well-ventilated fires, this is a good assumption. However, if a fire is in an under-ventilated compartment, or if a suppression agent like water mist or CO_2 is introduced, fuel and oxygen may mix but may not burn. Also, a shear layer with high strain rate separating the fuel stream from an oxygen supply can prevent combustion from taking place. The physical mechanisms underlying these phenomena are complex, and even simplified models still rely on a reasonably accurate estimation of the temperature and local strain rate in the neighborhood of the flame sheet. Sub-grid scale modeling of gas phase suppression and extinction is still an area of active research in the combustion community. Until reliable models can be developed for building-scale fire simulations, simple empirical rules can be devised that prevent burning from taking place when the atmosphere immediately surrounding the fire cannot sustain the combustion. Based on the work of Quintiere, Mowrer and others, a model for flame extinction has been implemented in FDS. The mixture fraction continues to be used to track the progress of the fuel mixing with the surrounding air, but now the surrounding volume is assessed to determine if it is more or less likely to support combustion. Figure 2 shows values of temperature and oxygen concentration for which burning can and cannot take place. Note that once the combustion region falls in the “No Burn” zone, the state relations (Fig. 1) are no longer valid for values of Z below stoichiometric, since now some fuel may be mixed with the other combustion products. To account for the deviation from the ideal state relations, at least one other scalar quantity in addition to the mixture fraction would have to be tracked in the calculation.

3.3 Finite-rate Reaction (DNS)

In a DNS calculation, the diffusion of fuel and oxygen can be modeled directly, thus it is possible to implement a relatively simple one-step chemical reaction. Consider the reaction of oxygen and a hydrocarbon fuel



The reaction rate is given by the expression

$$\frac{d[C_xH_y]}{dt} = -B [C_xH_y]^a [O_2]^b e^{-E/RT} \quad (46)$$

Suggested values of B , E , a and b for various hydrocarbon fuels are given in Refs. [16, 17]. It should be understood that the implementation of any of these one-step reaction schemes is still very much a research

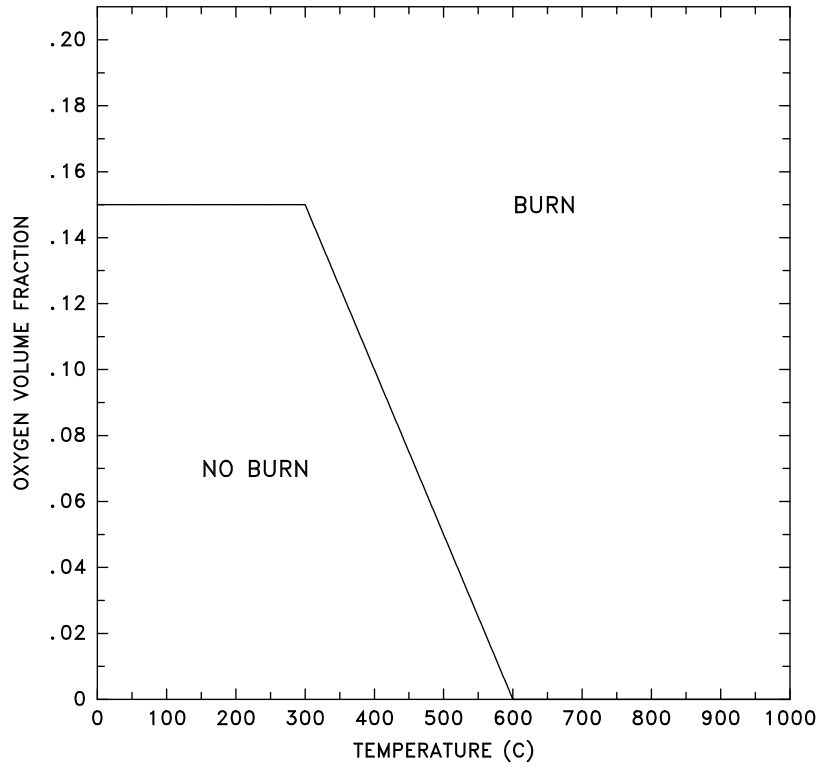


FIGURE 2: Oxygen-temperature phase space showing where combustion is allowed and not allowed to take place.

exercise because it is not universally accepted that combustion phenomena can be represented by such a simple mechanism. Efforts are currently underway to determine in what cases a one-step reaction mechanism provides a valid description of the combustion process.

4 Thermal Radiation

The Radiative Transport Equation (RTE) for an absorbing/emitting and scattering medium is

$$\mathbf{s} \cdot \nabla I_\lambda(\mathbf{x}, \mathbf{s}) = -[\kappa(\mathbf{x}, \lambda) + \sigma(\mathbf{x}, \lambda)] I(\mathbf{x}, \mathbf{s}) + B(\mathbf{x}, \lambda) + \frac{\sigma(\mathbf{x}, \lambda)}{4\pi} \int_{4\pi} \Phi(\mathbf{s}, \mathbf{s}') I_\lambda(\mathbf{x}, \mathbf{s}') d\Omega' \quad (47)$$

where $I_\lambda(\mathbf{x}, \mathbf{s})$ is the radiation intensity at wavelength λ , \mathbf{s} is the direction vector of the intensity, $\kappa(\mathbf{x}, \lambda)$ and $\sigma(\mathbf{x}, \lambda)$ are the local absorption and scattering coefficients, respectively, and $B(\mathbf{x}, \lambda)$ is the emission source term. The integral on the right hand side describes the in-scattering from other directions. In the case of a non-scattering gas the RTE becomes

$$\mathbf{s} \cdot \nabla I_\lambda(\mathbf{x}, \mathbf{s}) = \kappa(\mathbf{x}, \lambda) [I_b(\mathbf{x}) - I(\mathbf{x}, \mathbf{s})] \quad (48)$$

where $I_b(\mathbf{x})$ is the source term given by the Planck function. This section describes the radiation transport in the gas phase. The interaction of radiation with droplets is explained in Section 6.6.

In practical simulations the spectral dependence can not be solved accurately. Instead, the radiation spectrum is divided into a relatively small number of bands, and a separate RTE is derived for each band. The limits of the bands are selected to give an accurate representation of the most important radiation bands of CO₂ and water. The band specific RTE's are now

$$\mathbf{s} \cdot \nabla I_n(\mathbf{x}, \mathbf{s}) = \kappa_n(\mathbf{x}) [I_{b,n}(\mathbf{x}) - I(\mathbf{x}, \mathbf{s})], \quad n = 1 \dots N \quad (49)$$

where I_n is the intensity integrated over the band n , and κ_n is the appropriate mean absorption coefficient inside the band. The source term can be written as a fraction of the blackbody radiation

$$I_{b,n} = F_n(\lambda_{\min}, \lambda_{\max}) \sigma T^4 / \pi \quad (50)$$

where σ is the Stefan-Boltzmann constant. The calculation of factors F_n is explained in Ref. [18]. When the intensities corresponding to the bands are known, the total intensity is calculated by summing over all the bands

$$I(\mathbf{x}, \mathbf{s}) = \sum_{n=1}^N I_n(\mathbf{x}, \mathbf{s}) \quad (51)$$

From a series of numerical experiments it has been found that six bands are usually enough ($N = 6$). If the absorption of the fuel is known to be important, separate bands can be reserved for fuel, and the total number of bands is increased to ten ($N = 10$). For simplicity, the fuel is assumed to be CH₄. The limits of the bands are shown in Table 1.

TABLE 1: Limits of the spectral bands.

9 Band Model		1	2	3	4	5	6	7	8	9
Major Species		Soot	CO ₂ H ₂ O, Soot	CH ₄ Soot	Soot	CO ₂ Soot	H ₂ O Soot	H ₂ O CH ₄ , Soot	Soot	Soot
ν (1/cm)		10000	3800	3400	2800	2400	2174	1429	1160	1000
λ (μ m)		1.00	2.63	2.94	3.57	4.17	4.70	7.00	8.62	10.0
6 Band Model		1	2	3	4	5		6		
Major Species		Soot	CO ₂ H ₂ O, Soot	CH ₄ Soot	CO ₂ Soot	H ₂ O, CH ₄ , Soot		Soot		

Even with a reasonably small number of bands, the solution of N RTE's is very time consuming. Fortunately, in most large-scale fire scenarios soot is the most important combustion product controlling the

thermal radiation from the fire and hot smoke. As the radiation spectrum of soot is continuous, it is possible to assume that the gas behaves as a gray medium. The spectral dependence is lumped into one absorption coefficient ($N = 1$) and the source term is given by the blackbody radiation intensity

$$I_b(\mathbf{x}) = \sigma T(\mathbf{x})^4 / \pi \quad (52)$$

In optically thin flames, where the amount of soot is small compared to the amount of CO₂ and water, the gray gas assumption may produce significant overpredictions of the emitted radiation.

For the calculation of the gray or band-mean absorption coefficients, κ_n , a narrow-band model, Rad-Cal [19], has been implemented in FDS. At the start of a simulation the absorption coefficient(s) are tabulated as a function of mixture fraction and temperature. During the simulation the local absorption coefficient is found by table-lookup.

In calculations of limited spatial resolution, the source term, I_b , in the RTE requires special treatment in the neighborhood of the flame sheet because the temperatures are smeared out over a grid cell and are thus considerably lower than one would expect in a diffusion flame. Because of its dependence on the temperature raised to the fourth power, the source term must be modeled in those grid cells cut by the flame sheet. Elsewhere, there is greater confidence in the computed temperature, and the source term can assume its ideal value there

$$\kappa I_b = \begin{cases} \kappa \sigma T^4 / \pi & \text{Outside flame zone} \\ \chi_r \dot{q}''' / 4\pi & \text{Inside flame zone} \end{cases} \quad (53)$$

Here, \dot{q}''' is the chemical heat release rate per unit volume and χ_r is the *local* fraction of that energy emitted as thermal radiation. Note the difference between the prescription of a local χ_r and the resulting global equivalent. For a small fire ($D < 1$ m), the local χ_r is approximately equal to its global counterpart. However, as the fire increases in size, the global value will typically decrease due to a net re-absorption of the thermal radiation by the increasing smoke mantle.

The boundary condition for the radiation intensity leaving a gray diffuse wall is given as

$$I_w(\mathbf{s}) = \varepsilon I_{bw} + \frac{1 - \varepsilon}{\pi} \int_{\mathbf{s}' \cdot \mathbf{n}_w < 0} I_w(\mathbf{s}') |\mathbf{s}' \cdot \mathbf{n}_w| d\Omega \quad (54)$$

where $I_w(\mathbf{s})$ is the intensity at the wall, ε is the emissivity, and I_{bw} is the black body intensity at the wall.

The radiative transport equation (49) is solved using techniques similar to those for convective transport in finite volume methods for fluid flow [20], thus the name given to it is the Finite Volume Method (FVM). To obtain the discretized form of the RTE, the unit sphere is divided into a finite number of solid angles. In each grid cell a discretized equation is derived by integrating equation (48) over the cell ijk and the control angle $\delta\Omega^l$, to obtain

$$\int_{\Omega^l} \int_{V_{ijk}} \mathbf{s} \cdot \nabla I_n(\mathbf{x}, \mathbf{s}) dV d\Omega = \int_{\Omega^l} \int_{V_{ijk}} \kappa_n(\mathbf{x}) [I_{b,n}(\mathbf{x}) - I_n(\mathbf{x}, \mathbf{s})] dV d\Omega \quad (55)$$

The volume integral on the left hand side is replaced by a surface integral over the cell faces using the divergence theorem. Assuming that the radiation intensity $I(\mathbf{x}, \mathbf{s})$ is constant on each of the cell faces, the surface integral can be approximated by a sum over the cell faces. More detail on the discretization and solution of the RTE can be found in Section 7.7.

The radiant heat flux vector \mathbf{q}_r is defined

$$\mathbf{q}_r(\mathbf{x}) = \int \mathbf{s} I(\mathbf{x}, \mathbf{s}) d\Omega \quad (56)$$

The radiative loss term in the energy equation is

$$-\nabla \cdot \mathbf{q}_r(\mathbf{x}) = \kappa(\mathbf{x}) [U(\mathbf{x}) - 4\pi I_b(\mathbf{x})] \quad ; \quad U(\mathbf{x}) = \int_{4\pi} I(\mathbf{x}, \mathbf{s}) d\Omega \quad (57)$$

In words, the net radiant energy gained by a grid cell is the difference between that which is absorbed and that which is emitted.

5 Thermal Boundary Conditions

The type of thermal boundary condition applied at any given surface depends on whether that surface is to heat up and burn, whether the burning rate will simply be prescribed, or whether there is to be any burning at all.

5.1 Convective Heat Transfer to Walls

The heat fluxes to a solid surface consist of gains and losses from convection and radiation. The radiative flux at the surface is obtained from the boundary condition for the radiation equation, Eq. (54).

The calculation of the convective heat flux depends on whether one is performing a Direct Numerical Simulation (DNS) or a Large Eddy Simulation (LES). In a DNS calculation, the convective heat flux to a solid surface \dot{q}_c'' is obtained directly from the gas temperature gradient at the boundary

$$\dot{q}_c'' = -k \frac{\partial T}{\partial n} \quad (58)$$

where n is the spatial coordinate pointing into the solid. In an LES calculation, the convective heat flux to the surface is obtained from a combination of natural and forced convection correlations

$$\dot{q}_c'' = h \Delta T \quad \text{W/m}^2 \quad ; \quad h = \max \left[C |\Delta T|^{\frac{1}{3}} \quad , \quad \frac{k}{L} 0.037 \text{Re}^{\frac{4}{5}} \text{Pr}^{\frac{1}{3}} \right] \quad \text{W/m}^2/\text{K} \quad (59)$$

where ΔT is the difference between the wall and the gas temperature (taken at the center of the grid cell abutting the wall), C is the coefficient for natural convection (1.43 for a horizontal surface and 0.95 for a vertical surface) [21], L is a characteristic length related to the size of the physical obstruction, k is the thermal conductivity of the gas, and the Reynolds Re and Prandtl Pr numbers are based on the gas flowing past the obstruction. Since the Reynolds number is proportional to the characteristic length, L , the heat transfer coefficient is weakly related to L . For this reason, L is taken to be 1 m for most calculations.

5.2 Pyrolysis Model, Thermally-Thick Solid

If the surface material is assumed to be thermally-thick, a one-dimensional heat conduction equation for the material temperature, $T_s(n, t)$, is applied in the direction n pointing into the air/solid interface ($n = 0$)

$$\rho_s c_s \frac{\partial T_s}{\partial t} = k_s \frac{\partial^2 T_s}{\partial n^2} \quad ; \quad -k_s \frac{\partial T_s}{\partial n}(0, t) = \dot{q}_c'' + \dot{q}_r'' - \dot{m}'' \Delta H_v \quad (60)$$

where ρ_s , c_s and k_s are the (constant) density, specific heat and conductivity of the material; \dot{q}_c'' is the convective and \dot{q}_r'' is the (net) radiative heat flux at the surface, \dot{m}'' is the mass loss rate of fuel and ΔH_v is the heat of vaporization. It is assumed that fuel pyrolysis takes place at the surface, thus the heat required to vaporize fuel is extracted from the incoming energy flux. The pyrolysis rate is given by an Arrhenius expression

$$\dot{m}'' = A e^{-E/RT} \quad (61)$$

The value of the pre-exponential factor, A , is fixed, R is the universal gas constant, and E is adjusted so that the material burns in the neighborhood of a prescribed temperature. The actual burning rate is governed by the overall energy balance in the solid. These parameters are often difficult to obtain for real fuels; the intent of using the given expression for the mass loss rate is to mimic the behavior of burning objects when details of their pyrolysis mechanisms are unknown. Figure 3 displays a few plots of the mass flux versus temperature for two different temperatures.

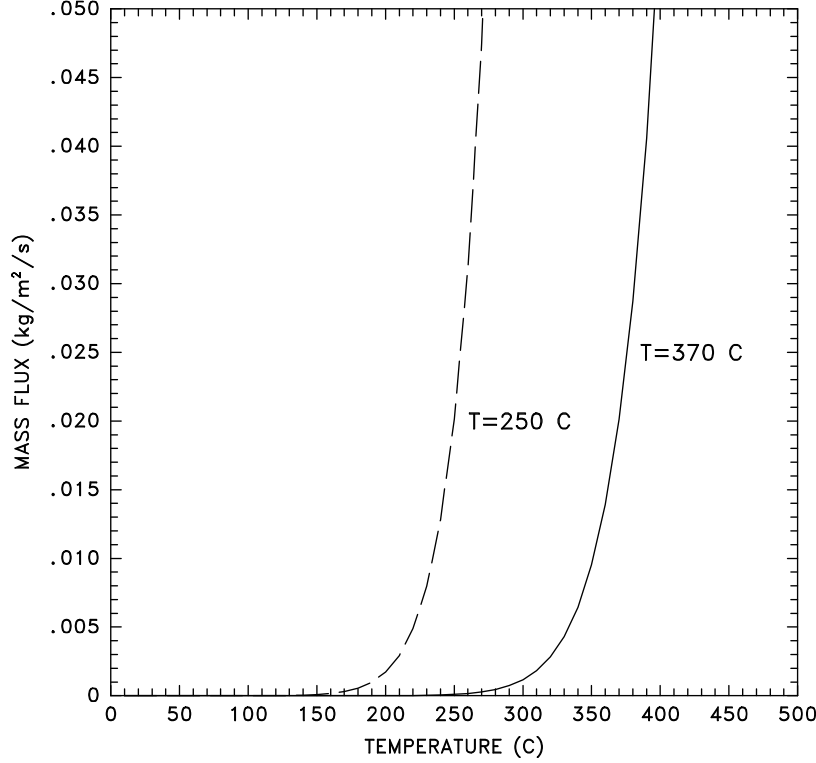


FIGURE 3: Fuel pyrolysis rates for two given “ignition” temperatures. See Eq. 61.

5.3 Pyrolysis Model, Thermally-Thin Solid

If the surface material is assumed to be thermally-thin, that is, its temperature is assumed uniform across its width, $T_s(t)$ is affected by gains and losses due to convection, radiation and pyrolysis. The thermal lag of the material is a function of the product of its density, specific heat and thickness δ

$$\frac{dT_s}{dt} = \frac{\dot{q}_c'' + \dot{q}_r'' - \dot{m}'' \Delta H_v}{\rho_s c_s \delta} \quad (62)$$

The convective and radiative fluxes are summed over the front and back surfaces of the thin fuel. Unless otherwise specified, the back surface is assumed to face an ambient temperature void. Note that the individual values of the parameters ρ_s , c_s and δ are not as important as their product, thus often in the literature and in the computer program, the three values are lumped together as a product. The pyrolysis rate for a thermally-thin fuel is the same as for a thermally-thick; see Eq. 61.

5.4 Pyrolysis Model, Liquid Fuels

The rate at which liquid fuel evaporates when burning is a function of the liquid temperature and the concentration of fuel vapor above the pool surface. Equilibrium is reached when the partial pressure of the fuel vapor above the surface equals the Clausius-Clapeyron pressure

$$p_{cc} = p_0 \exp \left[-\frac{h_v M_f}{\mathcal{R}} \left(\frac{1}{T_s} - \frac{1}{T_b} \right) \right] \quad (63)$$

where h_v is the heat of vaporization, M_f is the molecular weight, T_s is the surface temperature, and T_b is the boiling temperature of the fuel [22].

For simplicity, the liquid fuel itself is treated like a thermally-thick solid for the purpose of computing the heat conduction. There is no computation of the convection of the liquid within the pool.

6 Sprinklers

Simulating the effects of a sprinkler spray involves a number of pieces: predicting activation, computing the droplet trajectories and tracking the water as it drips onto the burning commodity.

6.1 Sprinkler Activation

The temperature of the sensing element of a given sprinkler is estimated from the differential equation put forth by Heskestad and Bill [23], with the addition of several terms to account for radiative heating and cooling by water droplets in the gas stream from previously activated sprinklers

$$\frac{dT_l}{dt} = \frac{\sqrt{|\mathbf{u}|}}{\text{RTI}}(T_g - T_l) - \frac{C}{\text{RTI}}(T_l - T_m) - \frac{C_2}{\text{RTI}}\beta|\mathbf{u}| \quad (64)$$

Here T_l is the link temperature, T_g is the gas temperature in the neighborhood of the link, T_m is the temperature of the sprinkler mount (assumed ambient), and β is the volume fraction of (liquid) water in the gas stream. The sensitivity of the detector is characterized by the value of RTI. The amount of heat conducted away from the link by the mount is indicated by the ‘‘C-Factor’’, C . The constant C_2 has been empirically determined by DiMarzo [24] to be $6 \times 10^6 \text{ K}/(\text{m/s})^{\frac{1}{2}}$, and its value is relatively constant for different types of sprinklers.

6.2 Sprinkler Droplet Size Distribution

Once activation is predicted, a sampled set of spherical water droplets is tracked from the sprinkler to either the floor or the burning commodity. In order to compute the droplet trajectories, the initial size and velocity of each droplet must be prescribed. This is done in terms of random distributions. The initial droplet size distribution of the sprinkler spray is expressed in terms of its Cumulative Volume Fraction (CVF), a function that relates the fraction of the water volume (mass) transported by droplets less than a given diameter. Researchers at Factory Mutual have suggested that the CVF for an industrial sprinkler may be represented by a combination of log-normal and Rosin-Rammler distributions [25]

$$F(d) = \begin{cases} \frac{1}{\sqrt{2\pi}} \int_0^d \frac{1}{\sigma d'} e^{-\frac{[\ln(d'/d_m)]^2}{2\sigma^2}} dd' & (d \leq d_m) \\ 1 - e^{-0.693(\frac{d}{d_m})^\gamma} & (d_m < d) \end{cases} \quad (65)$$

where d_m is the median droplet diameter (*i.e.* half the mass is carried by droplets with diameters of d_m or less), and γ and σ are empirical constants equal to about 2.4 and 0.6, respectively⁴. The median drop diameter is a function of the sprinkler orifice diameter, operating pressure, and geometry. Research at Factory Mutual has yielded a correlation for the median droplet diameter [26]

$$\frac{d_m}{D} \propto \text{We}^{-\frac{1}{3}} \quad (66)$$

where D is the orifice diameter of the sprinkler. The Weber number, the ratio of inertial forces to surface tension forces, is given by

$$\text{We} = \frac{\rho_w U^2 D}{\sigma_w} \quad (67)$$

where ρ_w is the density of water, U is the water discharge velocity, and σ_w is the water surface tension ($72.8 \times 10^{-3} \text{ N/m}$ at 20°C). The discharge velocity can be computed from the mass flow rate, which is a

⁴The Rosin-Rammler and log-normal distributions are smoothly joined if $\sigma = 2/(\sqrt{2\pi}(\ln 2)^\gamma) = 1.15/\gamma$.

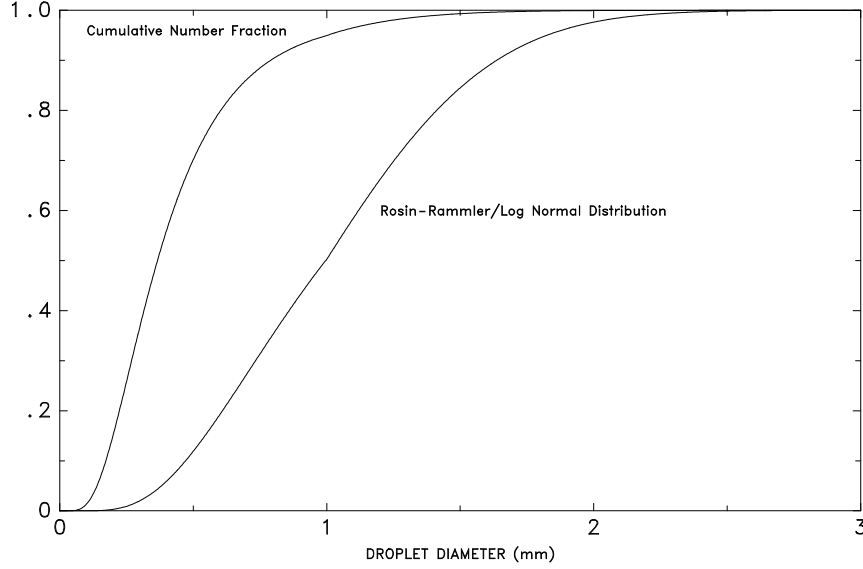


FIGURE 4: Cumulative Volume Fraction and Cumulative Number Fraction functions of the droplet size distribution from a typical industrial-scale sprinkler. The median diameter d_m is 1 mm, $\sigma = 0.6$ and $\gamma = 2.4$.

function of the sprinkler's operating pressure and K-Factor. FM reports that the constant of proportionality in Eq. (66) appears to be independent of flow rate and operating pressure. Three different sprinklers were tested in their study with orifice diameters of 16.3 mm, 13.5 mm, 12.7 mm and the constants were approximately 4.3, 2.9, 2.3, respectively. The strike plates of the two smaller sprinklers were notched, while that of the largest sprinkler was not [26].

In the numerical algorithm, the size of the sprinkler droplets are chosen to mimic the Rosin-Rammler/log-normal distribution. A Probability Density Function (PDF) for the droplet diameter is defined

$$f(d) = \frac{F'(d)}{d^3} \bigg/ \int_0^\infty \frac{F'(d')}{d'^3} dd' \quad (68)$$

Droplet diameters are randomly selected by equating the Cumulative Number Fraction of the droplet distribution with a uniformly distributed random variable U

$$U(d) = \int_0^d f(d') dd' \quad (69)$$

Figure 4 displays typical Cumulative Volume Fraction and Cumulative Number Fraction functions.

Every droplet from a given sprinkler is not tracked. Instead, a sampled set of the droplets is tracked. Typically, 1,000 droplets per sprinkler per second are tracked (50 droplets every 0.05 s, depending on user preference). The procedure for selecting droplet sizes is as follows: Suppose water is leaving the sprinkler at a mass flow rate of \dot{m} . Suppose also that the time interval for droplet insertion into the numerical simulation is δt , and the number of droplets inserted each time interval is N . Choose N uniformly distributed random numbers between 0 and 1, call them U_i , obtain N droplet diameters d_i based on the given droplet size distribution (Eq. (69)), and then compute a weighting constant C from the mass balance

$$\dot{m} \delta t = C \sum_{i=1}^N \frac{4}{3} \pi \rho_w \left(\frac{d_i}{2} \right)^3 \quad (70)$$

The mass and heat transferred from each droplet will be multiplied by the weighting factor C .

6.3 Sprinkler Droplet Trajectory in Air

For a sprinkler spray, the force term \mathbf{f} in Eq. (3) represents the momentum transferred from the water droplets to the gas. It is obtained by summing the force transferred from each droplet in a grid cell and dividing by the cell volume

$$\mathbf{f} = \frac{1}{2} \frac{\sum \rho C_D \pi r_d^2 (\mathbf{u}_d - \mathbf{u}) |\mathbf{u}_d - \mathbf{u}|}{\delta x \delta y \delta z} \quad (71)$$

where C_D is the drag coefficient, r_d is the droplet radius, \mathbf{u}_d is the velocity of the droplet, \mathbf{u} is the velocity of the gas, ρ is the density of the gas, and $\delta x \delta y \delta z$ is the volume of the grid cell. The trajectory of an individual droplet is governed by the equation

$$\frac{d}{dt}(m_d \mathbf{u}_d) = m_d \mathbf{g} - \frac{1}{2} \rho C_D \pi r_d^2 (\mathbf{u}_d - \mathbf{u}) |\mathbf{u}_d - \mathbf{u}| \quad (72)$$

where m_d is the mass of the droplet. The drag coefficient is a function of the local Reynolds number

$$C_D = \begin{cases} 24/\text{Re} & \text{Re} < 1 \\ 24(1 + 0.15 \text{Re}^{0.687})/\text{Re} & 1 < \text{Re} < 1000 \\ 0.44 & 1000 < \text{Re} \end{cases} \quad (73)$$

$$\text{Re} = \frac{\rho |\mathbf{u}_d - \mathbf{u}| 2r_d}{\mu} \quad (74)$$

where μ is the dynamic viscosity of air.

6.4 Sprinkler Droplet Transport on a Surface

When a water droplet hits a solid horizontal surface, it is assigned a random horizontal direction and moves at a fixed velocity until it reaches the edge, at which point it drops straight down at the same fixed velocity. This ‘‘dripping’’ velocity has been measured to be on the order of 0.5 m/s [27]. Penetration of water into porous materials is handled very crudely by assigning a fraction of the water droplets that strike a solid horizontal surface to go straight through the solid at a slow velocity. Neither the fraction nor the velocity has been validated.

6.5 Mass and Energy Transfer from Droplets

The evaporation of water droplets is handled semi-empirically. A water droplet suspended in air will evaporate as a function of the droplet equilibrium vapor mass fraction, the local gas phase vapor mass fraction, the heat transfer to the droplet, and the droplet’s motion relative to the gas. A correlation for the mass loss rate of a droplet that involves these parameters is given here [28]

$$\frac{dm_d}{dt} = -2\pi r_d \text{Sh} \rho D (Y_d - Y_g) \quad (75)$$

The subscripts d and g refer to the droplet and gas, respectively, m_d is the droplet mass, D is the diffusion coefficient for water vapor into air, Y is the water vapor mass fraction, and Sh is the droplet Sherwood number, given by a correlation involving the Reynolds and Schmidt numbers

$$\text{Sh} = 2 + 0.6 \text{Re}^{\frac{1}{2}} \text{Sc}^{\frac{1}{3}} \quad (76)$$

The vapor mass fraction of the gas, Y_g , is obtained from the overall set of mass conservation equations and the vapor mass fraction of the droplet is obtained from the Clausius-Clapeyron equation

$$X_d = \exp \left[\frac{h_v M_w}{\mathcal{R}} \left(\frac{1}{T_b} - \frac{1}{T_d} \right) \right] ; \quad Y_d = \frac{X_d}{X_d(1 - M_a/M_w) + M_a/M_w} \quad (77)$$

where X_d is the droplet water vapor volume fraction, h_v is the heat of vaporization, M_w is the molecular weight of water, M_a is the molecular weight of air, \mathcal{R} is the gas constant, T_b is the boiling temperature of water and T_d is the droplet temperature.

In addition to calculating the mass transfer due to evaporation, the transfer of energy must also be calculated. The droplet heats up due to the convective heat transfer across the surface of the droplet minus the energy required to evaporate water

$$m_d c_{p,w} \frac{dT_d}{dt} = A_d h_d (T_g - T_d) - \frac{dm_d}{dt} h_v \quad (78)$$

Here $c_{p,w}$ is the specific heat of water, $A_d = 4\pi r_d^2$ is the surface area of the droplet, h_d is the heat transfer coefficient, given by

$$h_d = \frac{\text{Nu } k}{2r_d} \quad ; \quad \text{Nu} = 2 + 0.6 \text{Re}^{\frac{1}{2}} \text{Pr}^{\frac{1}{3}} \quad (79)$$

Nu is the Nusselt number, k is the thermal conductivity of air, and the Prandtl number, Pr, is about 0.7 for air. The Sherwood number, Sh, is analogous to the Nusselt number, with the Schmidt number about 0.6 compared to the 0.7 for the Prandtl number.

Finally, the exchange of mass and energy between the droplets and the gas results in an additional term that must be added to the expression for the divergence, Eq. (8)

$$\nabla \cdot \mathbf{u} = \dots + \frac{\mathcal{R}}{\gamma p_0} \left(\rho \sum (Y_i/M_i) \frac{\partial T}{\partial t} + \frac{T}{M_w} \dot{m}_w''' \right) \quad (80)$$

where \dot{m}_w''' is the water evaporation rate per unit volume. The liquid water droplets are assumed to occupy no volume, simplifying the analysis.

6.6 Interaction of Droplets and Radiation

The attenuation of thermal radiation by water droplets is an important consideration, especially for water mist systems [29]. Water droplets attenuate thermal radiation through a combination of scattering and absorption [30]. The radiation-droplet interaction must therefore be solved for both the accurate prediction of the radiation field and for the droplet energy balance.

If the gas phase absorption and emission in Eq. (47) are temporarily neglected for simplicity, the radiative transport equation becomes

$$\mathbf{s} \cdot \nabla I_\lambda(\mathbf{x}, \mathbf{s}) = -[\kappa_d(\mathbf{x}, \lambda) + \sigma_d(\mathbf{x}, \lambda)] I(\mathbf{x}, \mathbf{s}) + \kappa_d(\mathbf{x}, \lambda) I_{b,d}(\mathbf{x}, \lambda) + \frac{\sigma_d(\mathbf{x}, \lambda)}{4\pi} \int_{4\pi} \Phi(\mathbf{s}, \mathbf{s}') I_\lambda(\mathbf{x}, \mathbf{s}') d\Omega' \quad (81)$$

where κ_d is the droplet absorption coefficient, σ_d is the droplet scattering coefficient and $I_{b,d}$ is the emission term of the droplets. $\Phi(\mathbf{s}, \mathbf{s}')$ is a scattering phase function that gives the scattered intensity from direction \mathbf{s}' to \mathbf{s} . The local absorption and scattering coefficients are calculated from the local droplet number density $N(\mathbf{x})$ and mean diameter $d_m(\mathbf{x})$ as

$$\begin{aligned} \kappa_d(\mathbf{x}, \lambda) &= N(\mathbf{x}) \int_0^\infty f(r, d_m(\mathbf{x})) C_a(r, \lambda) dr \\ \sigma_d(\mathbf{x}, \lambda) &= N(\mathbf{x}) \int_0^\infty f(r, d_m(\mathbf{x})) C_s(r, \lambda) dr \end{aligned} \quad (82)$$

where r is the droplet radius and C_a and C_s are absorption and scattering cross sections, respectively, given by Mie theory. The droplet number density function $f(r, d_m)$ is assumed to have the same form as the droplet size distribution, but a different mean.

An accurate computation of the in-scattering integral on the right hand side of Eq (81) would be extremely time consuming. It is here approximated by dividing the total 4π solid angle to a ‘‘forward angle’’

$\delta\Omega^l$ and “ambient angle” $\delta\Omega^* = 4\pi - \delta\Omega^l$. For compatibility with the FVM solver, $\delta\Omega^l$ is set equal to the control angle given by the angular discretization. However, it is assumed to be symmetric around the center of the control angle. Within $\delta\Omega^l$ the intensity is $I_\lambda(\mathbf{x}, \mathbf{s})$ and elsewhere it is approximated as

$$U^*(\mathbf{x}, \lambda) = \frac{U(\mathbf{x}, \lambda) - \delta\Omega^l I_\lambda(\mathbf{x}, \mathbf{s})}{\delta\Omega^*} \quad (83)$$

where $U(\mathbf{x})$ is the total integrated intensity. The in-scattering integral can now be written as

$$\frac{\sigma_d(\mathbf{x}, \lambda)}{4\pi} \int_{4\pi} \Phi(\mathbf{s}, \mathbf{s}') I_\lambda(\mathbf{x}, \mathbf{s}') d\Omega' = \sigma_d(\mathbf{x}, \lambda) [\chi_f I_\lambda(\mathbf{x}, \mathbf{s}) + (1 - \chi_f) U^*(\mathbf{x})] \quad (84)$$

where $\chi_f = \chi_f(r, \lambda)$ is a fraction of the total intensity originally within the solid angle $\delta\Omega^l$ that is scattered into the same angle $\delta\Omega^l$. Defining now an effective scattering coefficient section

$$\bar{\sigma}_d(\mathbf{x}, \lambda) = \frac{4\pi N(\mathbf{x})}{4\pi - \delta\Omega^l} \int_0^\infty (1 - \chi_f) C_s(r, \lambda) dr \quad (85)$$

the spray RTE becomes

$$\mathbf{s} \cdot \nabla I_\lambda(\mathbf{x}, \mathbf{s}) = -[\kappa_d(\mathbf{x}, \lambda) + \bar{\sigma}_d(\mathbf{x}, \lambda)] I(\mathbf{x}, \mathbf{s}) + \kappa_d(\mathbf{x}, \lambda) I_{b,d}(\mathbf{x}, \lambda) + \frac{\bar{\sigma}_d(\mathbf{x}, \lambda)}{4\pi} U(\mathbf{x}, \lambda) \quad (86)$$

This equation can be integrated over the spectrum to get the band specific RTE's. The procedure is exactly the same as what is used for the gas phase RTE. After the band integrations, the spray RTE for band n becomes

$$\mathbf{s} \cdot \nabla I_n(\mathbf{x}, \mathbf{s}) = -[\kappa_{d,n}(\mathbf{x}) + \bar{\sigma}_{d,n}(\mathbf{x})] I_n(\mathbf{x}, \mathbf{s}) + \kappa_{d,n}(\mathbf{x}) I_{b,d,n}(\mathbf{x}) + \frac{\bar{\sigma}_{d,n}(\mathbf{x})}{4\pi} U_n(\mathbf{x}) \quad (87)$$

where the source function is based on the average droplet temperature within a cell. The absorption and scattering cross sections and the scattering phase function are calculated using the MieV code developed by Wiscombe [31]. Both κ_d and $\bar{\sigma}_d$ are averaged over the possible droplet radii and wavelength before the actual simulation. A single constant temperature is used in the wavelength averaging. This “radiation temperature” T_{rad} should be selected to represent a typical radiating flame temperature. A value 1173 K is used by default. The averaged quantities, being now functions of the droplet mean diameter only, are saved in one-dimensional arrays. During the simulation, the local properties are calculated as a table lookup using the local mean droplet diameter [32]. Details of the computation are given in Section 7.8.

6.7 Fire Suppression by Water

The above two sections describe heat transfer from a droplet of water to a hot gas, a hot solid, or both. Although there is some uncertainty in the values of the respective heat transfer coefficients, the fundamental physics are fairly well understood. However, when the water droplets encounter burning surfaces, simple heat transfer correlations become more difficult to apply. The reason for this is that the water is not only cooling the surface and the surrounding gas, but it is also changing the pyrolysis rate of the fuel. If the surface of the fuel is planar, it is possible to characterize the decrease in the pyrolysis rate as a function of the decrease in the total heat feedback to the surface. Unfortunately, most fuels of interest in fire applications are multi-component solids with complex geometry at scales unresolvable by the computational grid.

To date, most of the work in this area has been performed at Factory Mutual. An important paper on the subject is by Yu *et al.* [33]. The authors consider dozens of rack storage commodity fires of different geometries and water application rates, and characterize the suppression rates in terms of a few global

parameters. Their analysis yields an expression for the total heat release rate from a rack storage fire after sprinkler activation

$$\dot{Q} = \dot{Q}_0 e^{-k(t-t_0)} \quad (88)$$

where \dot{Q}_0 is the total heat release rate at the time of application t_0 , and k is a fuel-dependent constant. For the FMRC Standard Plastic commodity k is given as

$$k = 0.716 \dot{m}_w'' - 0.0131 \quad \text{s}^{-1} \quad (89)$$

where \dot{m}_w'' is the flow rate of water impinging on the box tops, divided by the area of exposed surface (top and sides). It is expressed in units of kg/m²/s. For the Class II commodity, k is given as

$$k = 0.536 \dot{m}_w'' - 0.0040 \quad \text{s}^{-1} \quad (90)$$

Unfortunately, this analysis is based on global water flow and burning rates. Equation (88) accounts for both the cooling of non-burning surfaces as well as the decrease in heat release rate of burning surfaces. In the FDS model, the cooling of unburned surfaces and the reduction in the heat release rate are computed locally, thus it is awkward to apply a global suppression rule. However, the exponential nature of suppression by water is observed both locally and globally, thus it is assumed that the local burning rate of the fuel can be expressed in the form [27]

$$\dot{m}_f''(t) = \dot{m}_{f,0}''(t) e^{-\int k(t) dt} \quad (91)$$

Here $\dot{m}_{f,0}''(t)$ is the burning rate per unit area of the fuel when no water is applied and $k(t)$ is a linear function of the local water mass per unit area, m_w'' , expressed in units of kg/m²,

$$k(t) = a m_w''(t) \quad \text{s}^{-1} \quad (92)$$

Note that a is an empirical constant.

7 Numerical Method

This section presents the details of the numerical algorithm. First the equations that are being solved are presented. Each of the conservation equations emphasize the importance of the velocity divergence and vorticity fields, as well as the close relationship between the thermally expandable fluid equations [5] and the Boussinesq equations for which the authors have developed highly efficient solution procedures [34, 35]. All spatial derivatives are approximated by second order central differences and the flow variables are updated in time using an explicit second order predictor-corrector scheme.

7.1 Simplified Equations

Regardless of whether one is performing an LES or a DNS calculation, the overall solution algorithm is the same. The equations derived in Section 2 that are to be solved numerically are listed again here.

Conservation of Mass

$$\frac{\partial \rho}{\partial t} + \mathbf{u} \cdot \nabla \rho = -\rho \nabla \cdot \mathbf{u} \quad (93)$$

Conservation of Species

$$\frac{\partial \rho Y_i}{\partial t} + \mathbf{u} \cdot \nabla \rho Y_i = -\rho Y_i \nabla \cdot \mathbf{u} + \nabla \cdot \rho D \nabla Y_i + \dot{m}_i''' \quad (94)$$

Conservation of Momentum

$$\frac{\partial \mathbf{u}}{\partial t} + \mathbf{u} \times \boldsymbol{\omega} + \nabla \mathcal{H} = \frac{1}{\rho} ((\rho - \rho_\infty) \mathbf{g} + \mathbf{f} + \nabla \cdot \boldsymbol{\tau}) \quad (95)$$

Divergence Constraint

$$\nabla \cdot \mathbf{u} = \frac{1}{\rho c_p T} \left(\nabla \cdot k \nabla T + \nabla \cdot \sum_l \int c_{p,l} dT \rho D_l \nabla Y_l - \nabla \cdot \mathbf{q}_r + \dot{q}''' \right) + \left(\frac{1}{\rho c_p T} - \frac{1}{p_0} \right) \frac{dp_0}{dt} \quad (96)$$

Equation of State

$$p_0(t) = \rho T \mathcal{R} \sum_l Y_l / M_l \quad (97)$$

Notice that the source terms from the energy conservation equation have been incorporated into the divergence and ultimately are involved in the mass conservation equation. The temperature is found from the density and background pressure via the equation of state.

7.2 Temporal Discretization

All calculations start with ambient initial conditions. At the beginning of each time step, the quantities ρ^n , Y_i^n , \mathbf{u}^n , \mathcal{H}^n , and p_0^n are known. All other quantities can be derived from them. Note that the superscript $(n+1)_e$ refers to an estimate of the value of the quantities at the $(n+1)$ st time step.

1. The thermodynamic quantities ρ , Y_i , and p_0 are estimated at the next time step with an explicit Euler step. For example, the density is estimated

$$\rho^{(n+1)_e} = \rho^n - \delta t (\mathbf{u}^n \cdot \nabla \rho^n + \rho^n \nabla \cdot \mathbf{u}^n) \quad (98)$$

The divergence $(\nabla \cdot \mathbf{u})^{(n+1)_e}$ is formed from these estimated thermodynamic quantities. The normal velocity components at boundaries that are needed to form the divergence are assumed known.

2. A Poisson equation for the pressure is solved with a direct solver

$$\nabla^2 \mathcal{H}^n = -\frac{(\nabla \cdot \mathbf{u})^{(n+1)_e} - (\nabla \cdot \mathbf{u})^n}{\delta t} - \nabla \cdot \mathbf{F}^n \quad (99)$$

Note that the vector \mathbf{F} contains the convective, diffusive and force terms of the momentum equation. These will be described in detail below. Then the velocity is estimated at the next time step

$$\mathbf{u}^{(n+1)_e} = \mathbf{u}^n - \delta t (\mathbf{F}^n + \nabla \mathcal{H}^n) \quad (100)$$

Note that the divergence of the estimated velocity field is identically equal to the estimated divergence $(\nabla \cdot \mathbf{u})^{(n+1)_e}$ that was derived from the estimated thermodynamic quantities. The time step is checked at this point to ensure that

$$\delta t < \min \left(\frac{\delta x}{u}, \frac{\delta y}{v}, \frac{\delta z}{w} \right) \quad (101)$$

If the time step is too large, it is reduced so that it satisfies the CFL condition and the procedure starts from the beginning of the time step. If the time step satisfies the stability condition, the procedure continues.

3. The thermodynamic quantities ρ , Y_i , and p_0 are corrected at the next time step. For example, the density is corrected

$$\rho^{n+1} = \frac{1}{2} \left(\rho^n + \rho^{(n+1)_e} - \delta t (\mathbf{u}^{(n+1)_e} \cdot \nabla \rho^{(n+1)_e} + \rho^{(n+1)_e} \nabla \cdot \mathbf{u}^{(n+1)_e}) \right) \quad (102)$$

The divergence $(\nabla \cdot \mathbf{u})^{(n+1)}$ is derived from the corrected thermodynamic quantities.

4. The pressure is recomputed using estimated quantities

$$\nabla^2 \mathcal{H}^{(n+1)_e} = -\frac{2(\nabla \cdot \mathbf{u})^{n+1} - (\nabla \cdot \mathbf{u})^{(n+1)_e} - (\nabla \cdot \mathbf{u})^n}{\delta t} - \nabla \cdot \mathbf{F}^{(n+1)_e} \quad (103)$$

The velocity is then corrected

$$\mathbf{u}^{n+1} = \frac{1}{2} \left[\mathbf{u}^n + \mathbf{u}^{(n+1)_e} - \delta t \left(\mathbf{F}^{(n+1)_e} + \nabla \mathcal{H}^{(n+1)_e} \right) \right] \quad (104)$$

Note again that the divergence of the corrected velocity field is identically equal to the corrected divergence.

7.3 Spatial Discretization

Spatial derivatives in the governing equations are written as second order accurate finite differences on a rectilinear grid. The overall domain is a rectangular box that is divided into rectangular grid cells. Each cell is assigned indices i , j and k representing the position of the cell in the x , y and z directions, respectively. Scalar quantities are assigned in the center of each grid cell, thus ρ_{ijk}^n is the density at the n th time step in the center of the cell whose indices are i , j and k . Vector quantities like velocity are assigned at cell faces, thus the x component of velocity u is defined at the faces whose normals are parallel to the x -axis, the y component v is defined at the faces whose normals are parallel to the y -axis, and the z component w is defined at the faces whose normals are parallel to the z -axis. The quantity u_{ijk}^n is the x component of velocity at the forward pointing face of the ijk th cell; $u_{i-1,jk}^n$ is at the backward pointing face of the ijk th cell.

7.4 Large Eddy vs. Direct Numerical Simulation

The major difference between an LES and a DNS calculation is the form of the viscosity, and the thermal and material diffusivities. For a Large Eddy Simulation, the dynamic viscosity is defined at cell centers

$$\mu_{ijk} = \rho_{ijk} (C_s \Delta)^2 |S| \quad (105)$$

where C_s is an empirical constant, $\Delta = (\delta x \delta y \delta z)^{\frac{1}{3}}$, and

$$|S|^2 = 2 \left(\frac{\partial u}{\partial x} \right)^2 + 2 \left(\frac{\partial v}{\partial y} \right)^2 + 2 \left(\frac{\partial w}{\partial z} \right)^2 + \left(\frac{\partial u}{\partial y} + \frac{\partial v}{\partial x} \right)^2 + \left(\frac{\partial u}{\partial z} + \frac{\partial w}{\partial x} \right)^2 + \left(\frac{\partial v}{\partial z} + \frac{\partial w}{\partial y} \right)^2 - \frac{2}{3} (\nabla \cdot \mathbf{u})^2 \quad (106)$$

The quantity $|S|$ consists of second order spatial differences averaged at cell centers. The thermal conductivity and material diffusivity of the fluid are related to the viscosity by

$$k_{ijk} = \frac{c_{p,0} \mu_{ijk}}{\text{Pr}} \quad ; \quad (\rho D)_{ijk} = \frac{\mu_{ijk}}{\text{Sc}} \quad (107)$$

where Pr is the Prandtl number and Sc is the Schmidt number, both assumed constant. Note that the specific heat $c_{p,0}$ is that of the dominant species of the mixture. Based on simulations of smoke plumes, C_s is 0.14, Pr and Sc are 0.2. There is no rigorous justification for these choices.

The dynamic viscosity, thermal conductivity and diffusion coefficients for a DNS calculation are defined at cell centers

$$\mu_{ijk} = \sum_l Y_{l,ijk} \mu_l(T_{ijk}) \quad (108)$$

$$k_{ijk} = \sum_l Y_{l,ijk} k_l(T_{ijk}) \quad (109)$$

$$D_{l,ijk} = D_{l0}(T_{ijk}) \quad (110)$$

where the values for each individual species are approximated from kinetic theory [12]. The term D_{l0} is the binary diffusion coefficient for species l diffusing into the predominant species 0, usually nitrogen. It is often the case that the numerical grid is too coarse to resolve steep gradients in flow quantities when the temperature is near ambient. However, as the temperature increases and the diffusion coefficients increase in value, the situation improves. As a consequence, there is a provision in the numerical algorithm to place a lower bound on the viscous coefficients to avoid numerical instabilities at temperatures close to ambient.

7.5 The Mass Transport Equations

Due to the low Mach number approximation being used in the model, the mass and energy equations are combined by way of the divergence. The divergence of the flow field contains much of the fire-specific source terms described above.

7.5.1 Convective and Diffusive Transport

The density at the center of the ijk th cell is updated in time with the following predictor-corrector scheme. In the predictor step, the density at the $(n+1)$ st time level is estimated based on information at the n th level

$$\frac{\rho_{ijk}^{(n+1)e} - \rho_{ijk}^n}{\delta t} + (\mathbf{u} \cdot \nabla \rho)_{ijk}^n = -\rho_{ijk}^n (\nabla \cdot \mathbf{u})_{ijk}^n \quad (111)$$

Following the prediction of the velocity and background pressure at the $(n+1)$ st time level, the density is corrected

$$\frac{\rho_{ijk}^{(n+1)} - \frac{1}{2} (\rho_{ijk}^n + \rho_{ijk}^{(n+1)e})}{\frac{1}{2} \delta t} + (\mathbf{u} \cdot \nabla \rho)_{ijk}^{(n+1)e} = -\rho_{ijk}^{(n+1)e} (\nabla \cdot \mathbf{u})_{ijk}^{(n+1)e} \quad (112)$$

The species conservation equations are differenced the same way

$$\frac{(\rho Y_l)_{ijk}^{(n+1)e} - (\rho Y_l)_{ijk}^n}{\delta t} + (\mathbf{u} \cdot \nabla \rho Y_l)_{ijk}^n = -(\rho Y_l)_{ijk}^n (\nabla \cdot \mathbf{u})_{ijk}^n + (\nabla \cdot \rho D \nabla Y_l)_{ijk}^n + \dot{m}_{ijk}''' \quad (113)$$

at the predictor step, and

$$\frac{(\rho Y_l)_{ijk}^{(n+1)} - \frac{1}{2} ((\rho Y_l)_{ijk}^n + (\rho Y_l)_{ijk}^{(n+1)e})}{\frac{1}{2} \delta t} + (\mathbf{u} \cdot \nabla \rho Y_l)_{ijk}^{(n+1)e} = -(\rho Y_l)_{ijk}^{(n+1)e} (\nabla \cdot \mathbf{u})_{ijk}^{(n+1)e} + (\nabla \cdot \rho D \nabla Y_l)_{ijk}^{(n+1)e} + \dot{m}_{ijk}''' \quad (114)$$

at the corrector step.

The convective terms are written as upwind-biased differences in the predictor step and downwind-biased differences in the corrector step. In the expressions to follow, the symbol \pm means $+$ in the predictor step and $-$ in the corrector step. The opposite is true for \mp .

$$\begin{aligned} (\mathbf{u} \cdot \nabla \rho)_{ijk} = & \frac{1 \mp \varepsilon_u}{2} u_{ijk} \frac{\rho_{i+1,jk} - \rho_{ijk}}{\delta x} + \frac{1 \pm \varepsilon_u}{2} u_{i-1,jk} \frac{\rho_{ijk} - \rho_{i-1,jk}}{\delta x} + \\ & \frac{1 \mp \varepsilon_v}{2} v_{ijk} \frac{\rho_{i,j+1,k} - \rho_{ijk}}{\delta y} + \frac{1 \pm \varepsilon_v}{2} v_{i,j-1,k} \frac{\rho_{ijk} - \rho_{i,j-1,k}}{\delta y} + \\ & \frac{1 \mp \varepsilon_w}{2} w_{ijk} \frac{\rho_{ij,k+1} - \rho_{ijk}}{\delta z} + \frac{1 \pm \varepsilon_w}{2} w_{ij,k-1} \frac{\rho_{ijk} - \rho_{ij,k-1}}{\delta z} \end{aligned} \quad (115)$$

$$\begin{aligned} (\mathbf{u} \cdot \nabla \rho Y_l)_{ijk} = & \frac{1 \mp \varepsilon_u}{2} u_{ijk} \frac{(\rho Y_l)_{i+1,jk} - (\rho Y_l)_{ijk}}{\delta x} + \frac{1 \pm \varepsilon_u}{2} u_{i-1,jk} \frac{(\rho Y_l)_{ijk} - (\rho Y_l)_{i-1,jk}}{\delta x} + \\ & \frac{1 \mp \varepsilon_v}{2} v_{ijk} \frac{(\rho Y_l)_{i,j+1,k} - (\rho Y_l)_{ijk}}{\delta y} + \frac{1 \pm \varepsilon_v}{2} v_{i,j-1,k} \frac{(\rho Y_l)_{ijk} - (\rho Y_l)_{i,j-1,k}}{\delta y} + \\ & \frac{1 \mp \varepsilon_w}{2} w_{ijk} \frac{(\rho Y_l)_{ij,k+1} - (\rho Y_l)_{ijk}}{\delta z} + \frac{1 \pm \varepsilon_w}{2} w_{ij,k-1} \frac{(\rho Y_l)_{ijk} - (\rho Y_l)_{ij,k-1}}{\delta z} \end{aligned} \quad (116)$$

Note that without the inclusion of the ε 's, these are simple central difference approximations. The ε 's are local CFL numbers, $\varepsilon_u = u \delta t / \delta x$, $\varepsilon_v = v \delta t / \delta y$, and $\varepsilon_w = w \delta t / \delta z$, where the velocity components are those that immediately follow. Their role is to bias the differencing upwind. Where the local CFL number is near unity, the difference becomes nearly fully upwinded. Where the local CFL number is much less than unity, the differencing is more centralized [36].

7.6 Discretizing the Divergence

The divergence in both the predictor and corrector step is discretized

$$(\nabla \cdot \mathbf{u})_{ijk} = \frac{1}{\rho T c_p} \left(\dot{q}'''_{ijk} + (\nabla \cdot k \nabla T)_{ijk} + \sum_l (\nabla \cdot h_l \rho D \nabla Y_l)_{ijk} \right) + \left(\frac{1}{\rho T c_p} - \frac{1}{p_0} \right) \frac{dp_0}{dt} \quad (117)$$

The thermal and material diffusion terms are pure central differences, with no upwind or downwind bias, thus they are differenced the same way in both the predictor and corrector steps. For example, the thermal conduction term is differenced as follows:

$$\begin{aligned} (\nabla \cdot k \nabla T)_{ijk} = & \frac{1}{\delta x} \left[k_{i+\frac{1}{2},jk} \frac{T_{i+1,jk} - T_{ijk}}{\delta x} - k_{i-\frac{1}{2},jk} \frac{T_{ijk} - T_{i-1,jk}}{\delta x} \right] + \\ & \frac{1}{\delta y} \left[k_{i,j+\frac{1}{2},k} \frac{T_{i,j+1,k} - T_{ijk}}{\delta y} - k_{i,j-\frac{1}{2},k} \frac{T_{ijk} - T_{i,j-1,k}}{\delta y} \right] + \\ & \frac{1}{\delta z} \left[k_{ij,k+\frac{1}{2}} \frac{T_{ij,k+1} - T_{ijk}}{\delta z} - k_{ij,k-\frac{1}{2}} \frac{T_{ijk} - T_{ij,k-1}}{\delta z} \right] \end{aligned} \quad (118)$$

The temperature is extracted from the density via the equation of state

$$T_{ijk} = \frac{p_0}{\rho_{ijk} \mathcal{R} \sum_{l=0}^N (Y_{l,ijk} / M_l)} \quad (119)$$

Because only species 1 through N are explicitly computed, the summation is rewritten

$$\sum_{l=0}^N \frac{Y_{l,ijk}}{M_l} = \frac{1}{M_0} + \sum_{l=1}^N \left(\frac{1}{M_l} - \frac{1}{M_0} \right) Y_l \quad (120)$$

In isothermal calculations involving multiple species, the density can be extracted from the average molecular weight

$$\rho_{ijk} = \frac{p_0}{T_\infty \mathcal{R} \sum_{l=0}^N Y_{l,ijk} / M_l} \quad (121)$$

Again, because only species 1 through N are explicitly computed, this expression can be written

$$\rho_{ijk} = \frac{M_0 p_0}{T_\infty \mathcal{R}} + \sum_{l=1}^N \left(1 - \frac{M_0}{M_l} \right) (\rho Y_l)_{ijk} \quad (122)$$

7.6.1 Heat Release Rate (Mixture Fraction)

Energy from combustion is released into those grid cells through which the flame sheet ($Z = Z_f$) passes. The analytical expression for the heat release rate per unit area of flame sheet is

$$\dot{q}'' = \Delta H_O \left. \frac{dY_O}{dZ} \right|_{Z=Z_f} (\rho D) \nabla Z \cdot \mathbf{n} \quad (123)$$

where \mathbf{n} is the outward facing unit normal. Note that both dY_O/dZ and $\nabla Z \cdot \mathbf{n}$ are negative. To convert the analytical expression for the HRR per unit area into a discretized expression for the HRR per unit volume, all cells through which the flame sheet passes must be identified. Then, the normal derivative of Z must be computed component by component. For example, suppose the flame sheet passes between cell ijk and cell

$i + 1, jk$, and also suppose that $Z_{ijk} > Z_f > Z_{i+1,jk}$. The contribution to the heat release rate per unit volume in the ijk th and $i + 1, jk$ th cells from the small flame sheet is

$$\dot{q}''' = -\Delta H_O \left. \frac{dY_O}{dZ} \right|_{Z < Z_f} \frac{\left[(\rho D)_{i+\frac{1}{2},jk} (Z_{ijk} - Z_{i+1,jk}) / \delta x + u_{ijk} \rho_{i+\frac{1}{2},jk} (\bar{Z} - Z_f) \right] \delta y \delta z}{\delta x \delta y \delta z} \quad (124)$$

The distribution of energy is based on a linear interpolation of the value of the mixture fraction. A similar expression can be derived for all other possible cuts through the cell by the flame sheet. Note that the second term in the expression above corrects for error associated with locating the flame sheet. The terms above are a consequence of writing the convective and diffusive flux of fuel (mixture fraction) across the cell interface in conservative form:

$$u_{ijk} \frac{(\rho Z)_{i+1,jk} + (\rho Z)_{ijk}}{2} + (\rho D)_{i+\frac{1}{2},jk} \frac{Z_{ijk} - Z_{i+1,jk}}{\delta x} = u_{ijk} Z_f \rho_{i+\frac{1}{2},jk} + u_{ijk} (\bar{Z} - Z_f) \rho_{i+\frac{1}{2},jk} + (\rho D)_{i+\frac{1}{2},jk} \frac{Z_{ijk} - Z_{i+1,jk}}{\delta x} \quad (125)$$

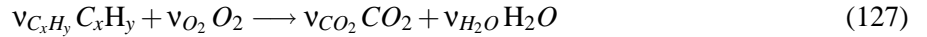
where

$$\bar{Z} = \frac{(\rho Z)_{i+1,jk} + (\rho Z)_{ijk}}{\rho_{i+1,jk} + \rho_{ijk}} \quad ; \quad \rho_{i+\frac{1}{2},jk} = \frac{\rho_{i+1,jk} + \rho_{ijk}}{2} \quad (126)$$

The second two terms on the right hand side constitute the ‘‘diffusive’’ flux, from which the heat release rate is derived.

7.6.2 Heat Release Rate (Finite-Rate Reaction)

In a DNS calculation (usually), a one-step, finite-rate reaction of a hydrocarbon fuel is assumed



For each grid cell, at the start of a time step where $t = t^n$ and $Y_{C_x H_y,ijk}^n \equiv Y_F(t^n)$ and $Y_{O_2,ijk}^n \equiv Y_O(t^n)$, the following ODE is solved numerically with a 2nd order Runge-Kutta scheme

$$\frac{dY_F}{dt} = -\frac{B \rho_{ijk}^{a+b-1}}{M_O^b M_F^{a-1}} Y_F(t)^a Y_O(t)^b e^{-E/RT_{ijk}} \quad (128)$$

$$\frac{dY_O}{dt} = -\frac{\nu_O M_O}{\nu_F M_F} \frac{dY_F}{dt} \quad (129)$$

The temperature T_{ijk} and density ρ_{ijk} are fixed at their values at time t^n and the ODE is iterated from t^n to t^{n+1} in about 100 time steps. The pre-exponential factor B , the activation energy E , and the exponents a and b are input parameters. The average heat release rate over the entire time step is given by

$$\dot{q}_{ijk}''' = \Delta H \rho_{ijk}^n \frac{Y_F(t^n) - Y_F(t^{n+1})}{\delta t} \quad (130)$$

where $\delta t = t^{n+1} - t^n$. The species mass fractions are adjusted at this point in the calculation (before the convection and diffusion update)

$$Y_{l,ijk}^n = Y_l(t^n) - \frac{\nu_l M_l}{\nu_F M_F} (Y_F(t^n) - Y_F(t^{n+1})) \quad (131)$$

7.7 Thermal Radiation

The discretized RTE is derived by integrating equation (48) over the grid cell ijk and the control angle $\delta\Omega^l$

$$\int_{\Omega^l} \int_{V_{ijk}} \mathbf{s} \cdot \nabla I(\mathbf{x}, \mathbf{s}) dV d\Omega = \int_{\Omega^l} \int_{V_{ijk}} \kappa(\mathbf{x}) [I_b(\mathbf{x}) - I(\mathbf{x}, \mathbf{s})] dV d\Omega \quad (132)$$

The volume integral on the left hand side is replaced by a surface integral over the cell faces using the divergence theorem. Assuming that the radiation intensity $I(\mathbf{x}, \mathbf{s})$ is constant on each of the cell faces, the surface integral can be approximated by a sum over the cell faces. Assuming further that $I(\mathbf{x}, \mathbf{s})$ is constant within the volume V_{ijk} and over the angle $\delta\Omega^l$ we obtain

$$\sum_{m=1}^6 A_m I_m^l \int_{\Omega^l} (\mathbf{s} \cdot \mathbf{n}_m) d\Omega = \kappa_{ijk} [I_{b,ijk} - I_{ijk}^l] V_{ijk} \delta\Omega^l \quad (133)$$

where

I_{ijk}^l	radiant intensity in direction l
I_m^l	radiant intensity at cell face m
$I_{b,ijk}$	radiant blackbody Intensity in cell
$\delta\Omega^l$	solid angle corresponding to direction l
V_{ijk}	volume of cell ijk
A_m	area of cell face m
\mathbf{n}_m	unit normal vector of the cell face m

It must be noticed, that while the intensity is assumed constant within the angle $\delta\Omega^l$, its direction covers the angle $\delta\Omega^l$ exactly.

In Cartesian coordinates⁵, the normal vectors \mathbf{n}_m are the base vectors of the coordinate system and the integrals over the solid angle do not depend on the physical coordinate, but the direction only. The intensities on the cell boundaries, I_m^l , are calculated using a first order upwind scheme. If the physical space is swept in the direction \mathbf{s}^l , the intensity I_{ijk}^l can be directly solved from an algebraic equation. This makes the numerical solution of the FVM very fast. Iterations are needed only to account for the reflective boundaries. However, this is seldom necessary in practice, because of the small time step set by the flow solver.

The spatial discretization for the RTE solver is the same as for the fluid solver. The coordinate system used to discretize the solid angle is shown in Figure 5. The discretization of the solid angle is done by dividing first the polar angle, θ , into N_θ bands, where N_θ is an even integer. Each θ -band is then divided into $N_\phi(\theta)$ parts in the azimuthal (ϕ) direction. $N_\phi(\theta)$ must be divisible by 4. The numbers N_θ and $N_\phi(\theta)$ are chosen to give the total number of angles N_Ω as close to the value defined by the user as possible. N_Ω is calculated as

$$N_\Omega = \sum_{i=1}^{N_\theta} N_\phi(\theta_i) \quad (134)$$

The distribution of the angles is based on empirical rules that try to produce equal solid angles $\delta\Omega^l = 4\pi/N_\Omega$. The number of θ -bands is

$$N_\theta = 1.17 N_\Omega^{1/2.26} \quad (135)$$

rounded to the nearest even integer. The number of ϕ -angles on each band is

$$N_\phi(\theta) = \max \{4, 0.5 N_\Omega [\cos(\theta^-) - \cos(\theta^+)]\} \quad (136)$$

⁵In the axisymmetric case equation (133) becomes a little bit more complicated, as the cell face normal vectors \mathbf{n}_m are not always constant. However, the computational efficiency can still be retained.

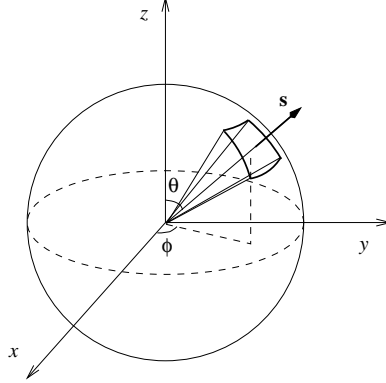


FIGURE 5: Coordinate system of the angular discretization.

rounded to the nearest integer that is divisible by 4. θ^- and θ^+ are the lower and upper bounds of the θ -band, respectively. The discretization is symmetric with respect to the planes $x = 0$, $y = 0$, and $z = 0$. This symmetry has three important benefits: First, it avoids the problems caused by the fact that first order upwind scheme, used to calculate intensities on the cell boundaries, is more diffusive in non-axial directions than axial. Second, the treatment of the mirror boundaries becomes very simple, as will be shown later. Third, it avoids so called “overhang” situations, where $\mathbf{s} \cdot \mathbf{i}$, $\mathbf{s} \cdot \mathbf{j}$ or $\mathbf{s} \cdot \mathbf{k}$ changes sign inside the control angle. These “overhangs” would make the resulting system of linear equations more complicated.

In the axially symmetric case these “overhangs” can not be avoided, and a special treatment, developed by Murthy and Mathur [37], is applied. In these cases $N_\phi(\theta_i)$ is kept constant, and the total number of angles is $N_\Omega = N_\theta \times N_\phi$. In addition, the angle of the vertical slice of the cylinder is chosen to be same as $\delta\phi$.

The cell face intensities, I_m^l , appearing on the left hand side of (133) are calculated using a first order upwind scheme. Consider, for example, a control angle having a direction vector \mathbf{s} . If the radiation is traveling in the positive x -direction, *i.e.* $\mathbf{s} \cdot \mathbf{i} \geq 0$, the intensity on the upwind side, I_{xu}^l is assumed to be the intensity in the neighboring cell, I_{i-1jk}^l , and the intensity on the downwind side is the intensity in the cell itself I_{ijk}^l .

On a rectilinear grid, the normal vectors \mathbf{n}_m are the base vectors of the coordinate system and the integrals over the solid angle can be calculated analytically. Equation (133) can be simplified

$$a_{ijk}^l I_{ijk}^l = a_x^l I_{xu}^l + a_y^l I_{yu}^l + a_z^l I_{zu}^l + b_{ijk}^l \quad (137)$$

where

$$a_{ijk}^l = A_x |D_x^l| + A_y |D_y^l| + A_z |D_z^l| + \kappa_{ijk} V_{ijk} \delta\Omega^l \quad (138)$$

$$a_x^l = A_x |D_x^l| \quad (139)$$

$$a_y^l = A_y |D_y^l| \quad (140)$$

$$a_z^l = A_z |D_z^l| \quad (141)$$

$$b_{ijk}^l = \kappa_{ijk} I_{b,ijk} V_{ijk} \delta\Omega^l \quad (142)$$

$$\delta\Omega^l = \int_{\Omega^l} d\Omega = \int_{\delta\phi} \int_{\delta\theta} \sin\theta \, d\theta \, d\phi \quad (143)$$

$$D_x^l = \int_{\Omega^l} (\mathbf{s}^l \cdot \mathbf{i}) d\Omega \quad (144)$$

$$\begin{aligned} &= \int_{\delta\phi} \int_{\delta\theta} (\mathbf{s}^l \cdot \mathbf{i}) \sin\theta \, d\theta d\phi \\ &= \int_{\delta\phi} \int_{\delta\theta} \cos\phi \sin\theta \sin\theta \, d\theta d\phi \\ &= \frac{1}{2} (\sin\phi^+ - \sin\phi^-) [\Delta\theta - (\cos\theta^+ \sin\theta^+ - \cos\theta^- \sin\theta^-)] \end{aligned}$$

$$D_y^l = \int_{\Omega^l} (\mathbf{s}^l \cdot \mathbf{j}) d\Omega \quad (145)$$

$$\begin{aligned} &= \int_{\delta\phi} \int_{\delta\theta} \sin\phi \sin\theta \sin\theta \, d\theta d\phi \\ &= \frac{1}{2} (\cos\phi^- - \cos\phi^+) [\Delta\theta - (\cos\theta^+ \sin\theta^+ - \cos\theta^- \sin\theta^-)] \end{aligned}$$

$$D_z^l = \int_{\Omega^l} (\mathbf{s}^l \cdot \mathbf{k}) d\Omega \quad (146)$$

$$\begin{aligned} &= \int_{\delta\phi} \int_{\delta\theta} \cos\theta \sin\theta \, d\theta d\phi \\ &= \frac{1}{2} \Delta\phi [(\sin\theta^+)^2 - (\sin\theta^-)^2] \end{aligned}$$

Here \mathbf{i} , \mathbf{j} and \mathbf{k} are the base vectors of the Cartesian coordinate system. θ^+ , θ^- , ϕ^+ and ϕ^- are the upper and lower boundaries of the control angle in the polar and azimuthal directions, respectively, and $\Delta\theta = \theta^+ - \theta^-$ and $\Delta\phi = \phi^+ - \phi^-$. The solution method of (137) is based on an explicit marching sequence [38]. The marching direction depends on the the propagation direction of the radiation intensity. As the marching is done in the “downwind” direction, the “upwind” intensities in all three spatial directions are known, and the intensity I_{ijk}^l can be solved directly. Iterations may be needed only with the reflective walls and optically thick situations. Currently, no iterations are made.

The boundary condition on a solid wall is given as

$$I_w^l = \varepsilon \frac{\sigma T_w^4}{\pi} + \frac{1-\varepsilon}{\pi} \sum_{D_w^{l'} < 0} I_w^{l'} |D_w^{l'}| \quad (147)$$

where $D_w^{l'} = \int_{\Omega^{l'}} (\mathbf{s} \cdot \mathbf{n}_w) d\Omega$. The constraint $D_w^{l'} < 0$ means that only the “incoming” directions are taken into account when calculating the reflection. The radiative heat flux on the wall is

$$q_w = \sum_{l=1}^{N_\Omega} I_w^l \int_{\delta\Omega^l} (\mathbf{s} \cdot \mathbf{n}_w) d\Omega = \sum_{l=1}^{N_\Omega} I_w^l D_n^l \quad (148)$$

where the coefficients D_n^l are equal to $\pm D_x^l$, $\pm D_y^l$ or $\pm D_z^l$, and can be calculated for each wall element beforehand.

The open boundaries are treated as black walls, where the incoming intensity is the black body intensity of the ambient temperature. On mirror boundaries the intensities leaving the wall are calculated from the incoming intensities using a predefined connection matrix.

$$I_{w,ijk}^l = I^l \quad (149)$$

Computationally intensive integration over all the incoming directions is avoided by keeping the solid angle discretization symmetric x , y and z planes. The connection matrix associates one incoming direction l' to each mirrored direction on each wall cell.

The local incident radiation intensity is

$$U_{ijk} = \sum_{l=1}^{N_\Omega} I_{ijk}^l \delta\Omega^l \quad (150)$$

7.8 Interaction of Droplets and Radiation

The computation of χ_f for a similar but simpler situation has been derived in Ref. [39]. It can be shown that here χ_f becomes

$$\chi_f = \frac{1}{\delta\Omega^l} \int_0^{\mu^l} \int_0^{\mu^l} \int_{\mu_{d,0}}^{\mu_{d,\pi}} \frac{P_0(\theta_d)}{(1-\mu^2)(1-\mu'^2) - (\mu_d - \mu\mu')^2} d\mu_d d\mu d\mu' \quad (151)$$

where μ_d is a cosine of the scattering angle θ_d and $P_0(\theta_d)$ is a single droplet scattering phase function

$$P_0(\theta_d) = \frac{\lambda^2 (|S_1(\theta_d)|^2 + |S_2(\theta_d)|^2)}{2C_s(r, \lambda)} \quad (152)$$

$S_1(\theta_d)$ and $S_2(\theta_d)$ are the scattering amplitudes, given by Mie-theory. The integration limit μ^l is a cosine of the polar angle defining the boundary of the symmetric control angle $\delta\Omega^l$

$$\mu^l = \cos(\theta^l) = 1 - \frac{2}{N_\Omega} \quad (153)$$

The limits of the innermost integral are

$$\mu_{d,0} = \mu\mu' + \sqrt{1-\mu^2}\sqrt{1-\mu'^2} \quad ; \quad \mu_{d,\pi} = \mu\mu' - \sqrt{1-\mu^2}\sqrt{1-\mu'^2} \quad (154)$$

When χ_f is integrated over the droplet size distribution to get an averaged value, it is multiplied by $C_s(r, \lambda)$. It is therefore $|S_1|^2 + |S_2|^2$, not $P_0(\theta_d)$, that is integrated. Physically, this means that intensities are added, not probabilities [31].

7.9 Thermal and Material Boundary Conditions

Four types of thermal boundary conditions are applied at solid surfaces. The first, and simplest, is an adiabatic boundary condition that states that there is no temperature gradient normal to the surface. It is implemented by assigning to the grid cell that is embedded in the solid (the ghost cell) the same temperature as the first cell in the gas (the gas cell).

The second type of boundary condition is where the solid surface has a prescribed temperature (usually this prescribed temperature is a function of time).

The third type of boundary condition assumes the solid to be thermally-thin. The surface temperature is updated in time according to

$$T_w^{n+1} = T_w^n + \delta t_s \frac{\dot{q}_c'' + \dot{q}_r''}{\rho_s c_s \delta} \quad (155)$$

where T_w is the wall temperature, δt_s is the time step used when updating the thermal boundary conditions (usually greater than the hydrodynamic time step δt), and ρ_s , c_s , δ are the input density, specific heat and thickness of the wall. In a DNS calculation where the boundary layer is resolved, the convective flux to the wall is given by

$$\dot{q}_c'' = -k \frac{T_{gas} - T_w}{\delta n/2} \quad (156)$$

where δn is the size of a grid cell in the normal direction to the wall. In an LES calculation where the boundary layer is not resolved,

$$\dot{q}_c'' = C|T_{gas} - T_w|^{\frac{1}{3}}(T_{gas} - T_w) \quad \text{W/m}^2 \quad (157)$$

where C is an empirical coefficient (0.95 for vertical surface; 1.43 for horizontal), and T_{gas} is the temperature of the gas in the cell bordering the wall.

The fourth type of thermal boundary condition is for a thermally-thick solid. In this case, a one dimensional heat transfer calculation is performed at each boundary cell designated as thermally-thick. The width of the solid δ is partitioned into N cells, clustered near the front face. The cell boundaries are located at points x_i

$$x_i = f(\xi_i) = \delta \frac{e^{s\xi_i/\delta} - 1}{e^s - 1} \quad (158)$$

where $0 \leq i \leq N$, $\xi_i = i\delta\xi$, $\delta\xi = \delta/N$, and $0 < s \leq 1$ is a measure of the degree of clustering of the cells at the front face. The width of each cell is $\delta x_i = f'(\xi_{i-\frac{1}{2}})\delta\xi$, $1 \leq i \leq N$ where $\xi_{i-\frac{1}{2}} = (i - \frac{1}{2})\delta\xi$. The temperature at the center of the i th cell is denoted $T_{s,i}$. These temperatures are updated in time using an implicit Crank-Nicholson scheme

$$\frac{T_{s,i}^{n+1} - T_{s,i}^n}{\delta t} = \frac{\alpha}{2\delta x_i} \left(\frac{T_{s,i+1}^n - T_{s,i}^n}{\delta x_{s,i+\frac{1}{2}}} - \frac{T_{s,i}^n - T_{s,i-1}^n}{\delta x_{s,i-\frac{1}{2}}} + \frac{T_{s,i+1}^{n+1} - T_{s,i}^{n+1}}{\delta x_{i+\frac{1}{2}}} - \frac{T_{s,i}^{n+1} - T_{s,i-1}^{n+1}}{\delta x_{i-\frac{1}{2}}} \right) \quad (159)$$

for $1 \leq i \leq N$. The boundary condition is discretized

$$-k_s \frac{T_{s,1}^{n+1} - T_{s,0}^{n+1}}{\delta x_{\frac{1}{2}}} = \dot{q}_c'' + \dot{q}_r'' - 4 \varepsilon \sigma T_{s,\frac{1}{2}}^3 (T_{s,\frac{1}{2}}^{n+1} - T_{s,\frac{1}{2}}^n) \quad (160)$$

where $T_{s,\frac{1}{2}} = (T_{s,1} + T_{s,0})/2$ is the temperature at the front face. Notice that the radiative emission term has been linearized

$$T_{s,\frac{1}{2}}^{(n+1)^4} - T_{s,\frac{1}{2}}^4 \approx 4 T_{s,\frac{1}{2}}^3 (T_{s,\frac{1}{2}}^{n+1} - T_{s,\frac{1}{2}}^n) \quad (161)$$

The wall temperature is defined $T_w \equiv T_{s,\frac{1}{2}} = (T_{s,0} + T_{s,1})/2$.

Regardless of how the wall temperature is determined, there are two ways of coupling the wall temperature with the fluid calculation. Gas phase temperatures are defined at cell centers; the wall is defined at the boundary of the bordering gas phase cell and a ‘‘ghost’’ cell inside the wall. As far as the gas phase calculation is concerned, the normal temperature gradient at the wall is expressed in terms of the temperature difference between the ‘‘gas’’ cell and the ‘‘ghost’’ cell. The wall temperature affects the gas phase calculation through the prescription of the ghost cell temperature. This ghost cell temperature has no physical meaning on its own. Only the difference between ghost and gas cell temperatures matters, for this defines the heat transfer to the wall. In a DNS calculation, the wall temperature is assumed to be an average of the ghost cell temperature and the temperature of the first cell in the gas, thus the ghost cell temperature is defined

$$T_{ghost} = 2T_w - T_{gas} \quad (162)$$

For an LES calculation, the heat lost to the boundary is equated with an empirical expression

$$k \frac{T_{gas} - T_{ghost}}{\delta n} = C|T_{gas} - T_w|^{\frac{1}{3}}(T_{gas} - T_w) \quad (163)$$

where δn is the distance between the center of the ghost cell and the center of the gas cell. This equation is solved for T_{ghost} , so that when the conservation equations are updated, the amount of heat lost to the wall is

equivalent to the empirical expression on the right hand side. Note that T_{ghost} is purely a numerical construct. It does not represent the temperature within the wall, but rather establishes a temperature gradient at the wall consistent with the empirical correlation.

At solid walls there is no transfer of mass, thus the boundary condition for the l th species at a wall is simply

$$Y_{l,ghost} = Y_{l,gas} \quad (164)$$

where the subscripts “ghost” and “gas” are the same as above since the mass fraction, like temperature, is defined at cell centers. At forced flow boundaries either the mass fraction $Y_{l,w}$ or the mass flux \dot{m}_l'' of species l may be prescribed. Then the ghost cell mass fraction can be derived because, as with temperature, the normal gradient of mass fraction is needed in the gas phase calculation. For cases where the mass fraction is prescribed

$$Y_{l,ghost} = 2Y_{l,w} - Y_{l,gas} \quad (165)$$

For cases where the mass flux is prescribed, the following equation must be solved iteratively

$$\dot{m}_l'' = u_n \frac{\rho_{ghost} Y_{l,ghost} + \rho_{gas} Y_{l,gas}}{2} - \rho D \frac{Y_{l,gas} - Y_{l,ghost}}{\delta n} \mp \frac{\delta t u_n^2}{2} \frac{\rho_{gas} Y_{l,gas} - \rho_{ghost} Y_{l,ghost}}{\delta n} \quad (166)$$

where \dot{m}_l'' is the mass flux of species l per unit area, u_n is the normal component of velocity at the wall pointing into the flow domain, and δn is the distance between the center of the ghost cell and the center of the gas cell. Notice that the last term on the right hand side is subtracted at the predictor step and added at the corrector step, consistent with the biased upwinding introduced earlier.

Once the temperature and species mass fractions have been defined in the ghost cell, the density in the ghost cell is computed from the equation of state

$$\rho_{ghost} = \frac{p_0}{\mathcal{R} T_{ghost} \sum_l (Y_{l,ghost} / M_l)} \quad (167)$$

7.10 The Momentum Equation

The three components of the momentum equation are

$$\frac{\partial u}{\partial t} + F_x + \frac{\partial \mathcal{H}}{\partial x} = 0 \quad ; \quad F_x = w\omega_y - v\omega_z - \frac{1}{\rho} \left(f_x + \frac{\partial \tau_{xx}}{\partial x} + \frac{\partial \tau_{xy}}{\partial y} + \frac{\partial \tau_{xz}}{\partial z} \right) \quad (168)$$

$$\frac{\partial v}{\partial t} + F_y + \frac{\partial \mathcal{H}}{\partial y} = 0 \quad ; \quad F_y = u\omega_z - w\omega_x - \frac{1}{\rho} \left(f_y + \frac{\partial \tau_{yx}}{\partial x} + \frac{\partial \tau_{yy}}{\partial y} + \frac{\partial \tau_{yz}}{\partial z} \right) \quad (169)$$

$$\frac{\partial w}{\partial t} + F_z + \frac{\partial \mathcal{H}}{\partial z} = 0 \quad ; \quad F_z = v\omega_x - u\omega_y - \frac{1}{\rho} \left(f_z + \frac{\partial \tau_{zx}}{\partial x} + \frac{\partial \tau_{zy}}{\partial y} + \frac{\partial \tau_{zz}}{\partial z} \right) \quad (170)$$

The spatial discretization of the momentum equations take the form

$$\frac{\partial u}{\partial t} + F_{x,ijk} + \frac{\mathcal{H}_{i+1,jk} - \mathcal{H}_{ijk}}{\delta x} = 0 \quad (171)$$

$$\frac{\partial v}{\partial t} + F_{y,ijk} + \frac{\mathcal{H}_{i,j+1,k} - \mathcal{H}_{ijk}}{\delta y} = 0 \quad (172)$$

$$\frac{\partial w}{\partial t} + F_{z,ijk} + \frac{\mathcal{H}_{ij,k+1} - \mathcal{H}_{ijk}}{\delta z} = 0 \quad (173)$$

where \mathcal{H}_{ijk} is taken at center of cell ijk , u_{ijk} and $F_{x,ijk}$ are taken at the side of the cell facing in the forward x direction, v_{ijk} and $F_{y,ijk}$ at the side facing in the forward y direction, and w_{ijk} and $F_{z,ijk}$ at the side facing in the forward z (vertical) direction. In the definitions to follow, the components of the vorticity ($\omega_x, \omega_y, \omega_z$) are located at cell edges pointing in the x, y and z directions, respectively. The same is true for the off-diagonal terms of the viscous stress tensor: $\tau_{zy} = \tau_{yz}$, $\tau_{xz} = \tau_{zx}$, and $\tau_{xy} = \tau_{yx}$. The diagonal components of the stress tensor τ_{xx} , τ_{yy} , and τ_{zz} ; the external force components (f_x, f_y, f_z); and the upwinding bias terms $\varepsilon_u, \varepsilon_v$, and ε_w are located at the respective cell faces.

$$\begin{aligned} F_{x,ijk} = & \left(\frac{1 \mp \varepsilon_w}{2} w_{i+\frac{1}{2},jk} \omega_{y,ijk} + \frac{1 \pm \varepsilon_w}{2} w_{i+\frac{1}{2},j,k-1} \omega_{y,ij,k-1} \right) \\ & - \left(\frac{1 \mp \varepsilon_v}{2} v_{i+\frac{1}{2},jk} \omega_{z,ijk} + \frac{1 \pm \varepsilon_v}{2} v_{i+\frac{1}{2},j-1,k} \omega_{z,i,j-1,k} \right) \\ & - \frac{1}{\rho_{i+\frac{1}{2},jk}} \left(f_{x,ijk} + \frac{\tau_{xx,i+1,jk} - \tau_{xx,ijk}}{\delta x} + \frac{\tau_{xy,ijk} - \tau_{xy,i,j-1,k}}{\delta y} + \frac{\tau_{xz,ijk} - \tau_{xz,i,j,k-1}}{\delta z} \right) \end{aligned} \quad (174)$$

$$\begin{aligned} F_{y,ijk} = & \left(\frac{1 \mp \varepsilon_u}{2} u_{i,j+\frac{1}{2},k} \omega_{z,ijk} + \frac{1 \pm \varepsilon_u}{2} u_{i-1,j+\frac{1}{2},k} \omega_{z,i-1,jk} \right) \\ & - \left(\frac{1 \mp \varepsilon_w}{2} w_{i,j+\frac{1}{2},k} \omega_{x,ijk} + \frac{1 \pm \varepsilon_w}{2} w_{i,j+\frac{1}{2},k-1} \omega_{x,ij,k-1} \right) \\ & - \frac{1}{\rho_{i,j+\frac{1}{2},k}} \left(f_{y,ijk} + \frac{\tau_{yx,ijk} - \tau_{yx,i-1,jk}}{\delta x} + \frac{\tau_{yy,i,j+1,k} - \tau_{yy,ijk}}{\delta y} + \frac{\tau_{yz,ijk} - \tau_{yz,i,j,k-1}}{\delta z} \right) \end{aligned} \quad (175)$$

$$\begin{aligned} F_{z,ijk} = & \left(\frac{1 \mp \varepsilon_v}{2} v_{ij,k+\frac{1}{2}} \omega_{x,ijk} + \frac{1 \pm \varepsilon_v}{2} v_{i,j-1,k+\frac{1}{2}} \omega_{x,i,j-1,k} \right) \\ & - \left(\frac{1 \mp \varepsilon_u}{2} u_{ij,k+\frac{1}{2}} \omega_{y,ijk} + \frac{1 \pm \varepsilon_u}{2} u_{i-1,j,k+\frac{1}{2}} \omega_{y,i-1,jk} \right) \\ & - \frac{1}{\rho_{ij,k+\frac{1}{2}}} \left(f_{z,ijk} + \frac{\tau_{zx,ijk} - \tau_{zx,i-1,jk}}{\delta x} + \frac{\tau_{zy,ijk} - \tau_{zy,i,j-1,k}}{\delta y} + \frac{\tau_{zz,ij,k+1} - \tau_{zz,ijk}}{\delta z} \right) \end{aligned} \quad (176)$$

$$\omega_{x,ijk} = \frac{w_{i,j+1,k} - w_{ijk}}{\delta y} - \frac{v_{ij,k+1} - v_{ijk}}{\delta z} \quad (177)$$

$$\omega_{y,ijk} = \frac{u_{i,j,k+1} - u_{ijk}}{\delta z} - \frac{w_{i+1,jk} - w_{ijk}}{\delta x} \quad (178)$$

$$\omega_{z,ijk} = \frac{v_{i+1,jk} - v_{ijk}}{\delta x} - \frac{u_{i,j+1,k} - u_{ijk}}{\delta y} \quad (179)$$

$$\tau_{xx,ijk} = \mu_{ijk} \left(2 \frac{u_{ijk} - u_{i-1,jk}}{\delta x} - \frac{2}{3} (\nabla \cdot \mathbf{u})_{ijk} \right) \equiv \mu_{ijk} \left(\frac{4}{3} (\nabla \cdot \mathbf{u})_{ijk} - 2 \frac{v_{ijk} - v_{i,j-1,k}}{\delta y} - 2 \frac{w_{ijk} - w_{ij,k-1}}{\delta z} \right) \quad (180)$$

$$\tau_{yy,ijk} = \mu_{ijk} \left(2 \frac{v_{ijk} - v_{i,j-1,k}}{\delta y} - \frac{2}{3} (\nabla \cdot \mathbf{u})_{ijk} \right) \equiv \mu_{ijk} \left(\frac{4}{3} (\nabla \cdot \mathbf{u})_{ijk} - 2 \frac{u_{ijk} - u_{i-1,jk}}{\delta x} - 2 \frac{w_{ijk} - w_{ij,k-1}}{\delta z} \right) \quad (181)$$

$$\tau_{zz,ijk} = \mu_{ijk} \left(2 \frac{w_{ijk} - w_{ij,k-1}}{\delta z} - \frac{2}{3} (\nabla \cdot \mathbf{u})_{ijk} \right) \equiv \mu_{ijk} \left(\frac{4}{3} (\nabla \cdot \mathbf{u})_{ijk} - 2 \frac{u_{ijk} - u_{i-1,jk}}{\delta x} - 2 \frac{v_{ijk} - v_{i,j-1,k}}{\delta y} \right) \quad (182)$$

$$\tau_{xy,ijk} = \tau_{yx,ijk} = \mu_{i+\frac{1}{2},j+\frac{1}{2},k} \left(\frac{u_{i,j+1,k} - u_{ijk}}{\delta y} + \frac{v_{i+1,jk} - v_{ijk}}{\delta x} \right) \quad (183)$$

$$\tau_{xz,ijk} = \tau_{zx,ijk} = \mu_{i+\frac{1}{2},j,k+\frac{1}{2}} \left(\frac{u_{i,j,k+1} - u_{ijk}}{\delta z} + \frac{w_{i+1,jk} - w_{ijk}}{\delta x} \right) \quad (184)$$

$$\tau_{yz,ijk} = \tau_{zy,ijk} = \mu_{i,j+\frac{1}{2},k+\frac{1}{2}} \left(\frac{v_{i,j,k+1} - v_{ijk}}{\delta z} + \frac{w_{i,j+1,k} - w_{ijk}}{\delta y} \right) \quad (185)$$

$$\varepsilon_u = \frac{u \delta t}{\delta x} \quad (186)$$

$$\varepsilon_v = \frac{v \delta t}{\delta y} \quad (187)$$

$$\varepsilon_w = \frac{w \delta t}{\delta z} \quad (188)$$

The variables ε_u , ε_v and ε_w are local CFL numbers evaluated at the same locations as the velocity component immediately following them, and serve to bias the differencing of the convective terms in the upwind direction. The subscript $i + \frac{1}{2}$ indicates that a variable is an average of its values at the i th and the $(i + 1)$ th cell. The divergence defined in Eq. (117) is identically equal to the divergence defined by

$$(\nabla \cdot \mathbf{u})_{ijk} = \frac{u_{ijk} - u_{i-1,jk}}{\delta x} + \frac{v_{ijk} - v_{i,j-1,k}}{\delta y} + \frac{w_{ijk} - w_{ij,k-1}}{\delta z} \quad (189)$$

The equivalence of the two definitions of the divergence is a result of the form of the discretized equations, the time-stepping scheme, and the direct solution of the Poisson equation for the pressure.

7.10.1 Force Terms

The external force term components, in addition to including the effects of buoyancy, may also include the drag force from sprinkler droplets.

$$f_{x,ijk} = \frac{1}{2} \frac{\sum \rho C_D \pi r_d^2 (u_d - u_{ijk}) |\mathbf{u}_d - \mathbf{u}|}{\delta x \delta y \delta z} - (\rho_{i+\frac{1}{2},jk} - \rho_\infty) g_x \quad (190)$$

$$f_{y,ijk} = \frac{1}{2} \frac{\sum \rho C_D \pi r_d^2 (v_d - v_{ijk}) |\mathbf{u}_d - \mathbf{u}|}{\delta x \delta y \delta z} - (\rho_{i,j+\frac{1}{2},k} - \rho_\infty) g_y \quad (191)$$

$$f_{z,ijk} = \frac{1}{2} \frac{\sum \rho C_D \pi r_d^2 (w_d - w_{ijk}) |\mathbf{u}_d - \mathbf{u}|}{\delta x \delta y \delta z} - (\rho_{i,j,k+\frac{1}{2}} - \rho_\infty) g_z \quad (192)$$

where $\mathbf{g} = (g_x, g_y, g_z)$ is the gravity vector, r_d is the radius of a droplet, $\mathbf{u} = (u_d, v_d, w_d)$ the velocity of a droplet, C_D the drag coefficient, and $\delta x \delta y \delta z$ the volume of the ijk th cell. The summations represent all droplets within a grid cell centered about the x , y and z faces of a grid cell respectively.

7.10.2 Time Step

The time step is determined by the CFL condition, and in cases of high viscosity, a parabolic stability criterion typical of explicit second order accurate schemes

$$\delta t < \min \left(\frac{\delta x}{u_{ijk}}, \frac{\delta y}{v_{ijk}}, \frac{\delta z}{w_{ijk}}, \frac{\rho_{ijk} \delta x^2}{8\mu_{ijk}}, \frac{\rho_{ijk} \delta y^2}{8\mu_{ijk}}, \frac{\rho_{ijk} \delta z^2}{8\mu_{ijk}} \right) \quad (193)$$

The estimated velocities $u^{(n+1)e}$, $v^{(n+1)e}$ and $w^{(n+1)e}$ are tested at each time step to ensure that the above condition is satisfied. If it is not, then the time step is set to 0.8 of its allowed maximum value and the estimated velocities are recomputed (and checked again). The parabolic stability criterion is only invoked for a DNS calculation.

7.11 The Pressure Equation

The divergence of the momentum equation yields a Poisson equation for the pressure

$$\begin{aligned} & \frac{\mathcal{H}_{i+1,jk} - 2\mathcal{H}_{ijk} + \mathcal{H}_{i-1,jk}}{\delta x^2} + \frac{\mathcal{H}_{i,j+1,k} - 2\mathcal{H}_{ijk} + \mathcal{H}_{i,j-1,k}}{\delta y^2} + \frac{\mathcal{H}_{i,j,k+1} - 2\mathcal{H}_{ijk} + \mathcal{H}_{i,j,k-1}}{\delta z^2} \\ & = -\frac{F_{x,ijk} - F_{x,i-1,jk}}{\delta x} - \frac{F_{y,ijk} - F_{y,i,j-1,k}}{\delta y} - \frac{F_{z,ijk} - F_{z,i,j,k-1}}{\delta z} - \frac{\partial}{\partial t}(\nabla \cdot \mathbf{u})_{ijk} \end{aligned} \quad (194)$$

The lack of a superscript implies that all quantities are to be evaluated at the same time level. This elliptic partial differential equation is solved using a direct (non-iterative) FFT-based solver that is part of a library of routines for solving elliptic PDEs called CRAYFISHPAK [40]. To ensure that the divergence of the fluid is consistent with the definition given in Eq. (8), the time derivative of the divergence is defined

$$\frac{\partial}{\partial t}(\nabla \cdot \mathbf{u})_{ijk} = \frac{(\nabla \cdot \mathbf{u})_{ijk}^{(n+1)e} - (\nabla \cdot \mathbf{u})_{ijk}^n}{\delta t} \quad (195)$$

at the predictor step, and then

$$\frac{\partial}{\partial t}(\nabla \cdot \mathbf{u})_{ijk} = \frac{2(\nabla \cdot \mathbf{u})_{ijk}^{n+1} - (\nabla \cdot \mathbf{u})_{ijk}^{(n+1)e} - (\nabla \cdot \mathbf{u})_{ijk}^n}{\delta t} \quad (196)$$

at the corrector step. The discretization of the divergence was given in Eq. (117).

Direct Poisson solvers are most efficient if the domain is a rectangular region, although other geometries such as cylinders and spheres can be handled almost as easily. For these solvers, the no-flux condition (197) is simple to prescribe at external boundaries. For example, at the floor, $z = 0$, the Poisson solver is supplied with the Neumann boundary condition

$$\frac{\mathcal{H}_{i,j,1} - \mathcal{H}_{i,j,0}}{\delta z} = -F_{z,ij,0} \quad (197)$$

However, many practical problems involve more complicated geometries. For building fires, doors and windows within multi-room enclosures are very important features of the simulations. These elements may be included in the overall domain as masked grid cells, but the no-flux condition (197) cannot be directly prescribed at the boundaries of these blocked cells. Fortunately, it is possible to exploit the relatively small changes in the pressure from one time step to the next to enforce the no-flux condition. At the start of a time step, the components of the convection/diffusion term \mathbf{F} are computed at all cell faces that do not correspond to walls. At those cell faces that do correspond to solid walls, prescribe

$$F_n = -\frac{\partial \mathcal{H}^*}{\partial n} + \beta u_n \quad (198)$$

where F_n is the normal component of \mathbf{F} at the wall, and β is a relaxation factor empirically determined to be about 0.8 divided by the time step δt . The asterisk indicates the most recent value of the pressure. Obviously, the pressure at this particular time step is not known until the Poisson equation is solved. Equation (198) asserts that following the solution of the Poisson equation for the pressure, the normal component of velocity u_n will be driven closer to zero according to

$$\frac{\partial u_n}{\partial t} \approx -\beta u_n \quad (199)$$

This is approximate because the true value of the velocity time derivative depends on the solution of the pressure equation, but since the most recent estimate of pressure is used, the approximation is very good. Also, even though there are small errors in normal velocity at solid surfaces, the divergence of each blocked cell remains exactly zero for the duration of the calculation. In other words, the total flux into a given obstruction is always identically zero, and the error in normal velocity is usually at least several orders of magnitude smaller than the characteristic flow velocity. When implemented as part of a predictor-corrector updating scheme, the no-flux condition at solid surfaces is maintained remarkably well.

At open boundaries (say $i = I$), \mathcal{H} is prescribed depending on whether the flow is incoming or outgoing

$$\begin{aligned} \mathcal{H}_{I+\frac{1}{2},jk} &= (u_{I,jk}^2 + v_{I,j-\frac{1}{2},k}^2 + w_{I,j-\frac{1}{2},k}^2)/2 & u_{I,jk} > 0 \\ \mathcal{H}_{I+\frac{1}{2},jk} &= 0 & u_{I,jk} < 0 \end{aligned} \quad (200)$$

where I is the index of the last gas phase cell in the x direction and $u_{I,jk}$ is the x component of velocity at the boundary. The value of H in the ghost cell is

$$\mathcal{H}_{I+1,jk} = 2\mathcal{H}_{I+\frac{1}{2},jk} - \mathcal{H}_{I,jk} \quad (201)$$

7.12 Particle Tracking

Thermal elements are introduced into the flow field as a means of introducing heat and as a way to visualize the flow. The position \mathbf{x}_p of each thermal element is governed by the equations

$$\frac{d\mathbf{x}_p}{dt} = \mathbf{u} \quad (202)$$

The thermal element positions are updated according to the same predictor-corrector scheme that is applied to the other flow quantities. Briefly, the position \mathbf{x}_p of a given thermal element is updated according to the two step scheme

$$\mathbf{x}_p^{(n+1)e} = \mathbf{x}_p^n + \delta t \bar{\mathbf{u}}^n \quad (203)$$

$$\mathbf{x}_p^{n+1} = \frac{1}{2} \left(\mathbf{x}_p^n + \mathbf{x}_p^{(n+1)e} + \delta t \bar{\mathbf{u}}^{(n+1)e} \right) \quad (204)$$

where the bar over the velocity vector indicates that the velocity of the fluid is interpolated at the element's position.

8 Conclusion

The equations and numerical algorithm described in this document form the core of an evolving fire model. As research into specific fire-related phenomena continues, the relevant parts of the model can be improved. Because the model was originally designed to analyze industrial-scale fires, it can be used reliably when the fire size is specified and the building is relatively large in relation to the fire. In these cases, the model predicts flow velocities and temperatures to an accuracy of 10 to 20% compared to experimental measurements. Currently, research is focussed on improving both the gas phase and solid phase descriptions of combustion in the model so that simulations involving fire growth and suppression, especially in residential sized rooms, can be improved.

Any user of the numerical model must be aware of the assumptions and approximations being employed. There are two issues for any potential user to consider before embarking on calculations. First, for both real and simulated fires, the growth of the fire is very sensitive to the thermal properties (conductivity, specific heat, density, burning rate, *etc.*) of the surrounding materials. Second, even if all the material properties are known, the physical phenomena of interest may not be simulated due to limitations in the model algorithms or numerical grid. Except for those few materials that have been studied to date at NIST, the user must supply the thermal properties of the materials, and then validate the performance of the model with experiments to ensure that the model has the necessary physics included. Only then can the model be expected to predict the outcome of fire scenarios that are similar to those that have actually been tested.

9 Nomenclature

A_s	water droplet surface area
B	pre-exponential factor for Arrhenius reaction
C	Sprinkler C-Factor
C_D	drag coefficient
C_s	Smagorinsky constant (LES)
c_p	constant pressure specific heat
D	diffusion coefficient
D^*	characteristic fire diameter
d_m	median volumetric droplet diameter
E	activation energy
\mathbf{f}	external force vector (excluding gravity)
g	acceleration of gravity
\mathcal{H}	total pressure divided by the density
h	enthalpy; heat transfer coefficient
h_i	enthalpy of i th species
h_i^0	heat of formation of i th species
I	radiation intensity
I_b	radiation blackbody intensity
k	thermal conductivity; suppression decay factor
M	molecular weight of the gas mixture
M_i	molecular weight of i th gas species
\dot{m}_f''	fuel mass flux
\dot{m}_w''	water mass flux
m_w''	water mass per unit area
\dot{m}_O''	oxygen consumption rate per unit area
Nu	Nusselt number
Pr	Prandtl number
p	pressure
p_0	background pressure
\tilde{p}	pressure perturbation
\mathbf{q}_r	radiative heat flux vector
\dot{q}'''	heat release rate per unit volume
\dot{q}_r''	radiative flux to a solid surface
\dot{q}_c''	convective flux to a solid surface
\dot{Q}	total heat release rate
Q^*	characteristic fire size
\mathcal{R}	universal gas constant
Re	Reynolds number
r_d	water droplet radius
RTI	Response Time Index of sprinkler
\mathbf{s}	unit vector in direction of radiation intensity
Sc	Schmidt number
Sh	Sherwood number
T	temperature
t	time
t_b	thermal element burn-out time (LES)

U	integrated radiant intensity
$\mathbf{u} = (u, v, w)$	velocity vector
\dot{m}_i'''	production rate of i th species per unit volume
We	Weber number
$\mathbf{x} = (x, y, z)$	position vector
X_i	volume fraction of i th species
Y_i	mass fraction of i th species
Y_O^∞	mass fraction of oxygen in the ambient
Y_F^I	mass fraction of fuel in the fuel stream
y_s	soot yield
Z	mixture fraction
γ	ratio of specific heats; Rosin-Rammler exponent
ΔH	heat of combustion
ΔH_O	energy released per unit mass oxygen consumed
δ	wall thickness
κ	absorption coefficient
μ	dynamic viscosity
ν_i	stoichiometric coefficient, species i
Φ	dissipation function
ρ	density
τ	viscous stress tensor
χ_r	radiative loss fraction
σ	Stefan-Boltzmann constant
$\boldsymbol{\omega} = (\omega_x, \omega_y, \omega_z)$	vorticity vector

References

- [1] H.C. Hottel. Stimulation of Fire Research in the United States After 1940. *Combustion Science and Technology*, 39:1–10, 1984.
- [2] J. Quintiere. A Perspective on Compartment Fire Growth. *Combustion Science and Technology*, 39:11–54, 1984.
- [3] G.P. Forney and W.F. Moss. Analyzing and Exploiting Numerical Characteristics of Zone Fire Models. *Fire Science and Technology*, 14:49–60, 1994.
- [4] S.V. Patankar. *Numerical Heat Transfer and Fluid Flow*. Hemisphere Publishing, New York, 1980.
- [5] R.G. Rehm and H.R. Baum. The Equations of Motion for Thermally Driven, Buoyant Flows. *Journal of Research of the NBS*, 83:297–308, 1978.
- [6] H.R. Baum and K.B. McGrattan. Simulation of Large Industrial Outdoor Fires. In *Fire Safety Science – Proceedings of the Sixth International Symposium*. International Association for Fire Safety Science, 1999.
- [7] J. Smagorinsky. General Circulation Experiments with the Primitive Equations. I. The Basic Experiment. *Monthly Weather Review*, 91:99–164, 1963.
- [8] J.W. Deardorff. Numerical Investigation of Neutral and Unstable Planetary Boundary Layers. *Journal of Atmospheric Sciences*, 29:91–115, 1972.
- [9] M. Germano, U. Piomelli, P. Moin, and W.H. Cabot. A Dynamic Subgrid-Scale Eddy Viscosity Model. *Physics of Fluids A*, 3:1760–1765, 1991.
- [10] D.K. Lilly. A Proposed Modification of the Germano Subgrid-Scale Closure Method. *Physics of Fluids A*, 4:633–635, 1992.
- [11] H.R. Baum, K.B. McGrattan, and R.G. Rehm. Three Dimensional Simulations of Fire Plume Dynamics. *Journal of the Heat Transfer Society of Japan*, 35:45–52, 1997.
- [12] R.C. Reid, J.M. Prausnitz, and B.E. Poling. *Properties of Gases and Liquids*. McGraw-Hill, Inc., New York, 4th edition, 1987.
- [13] C. Huggett. Estimation of the Rate of Heat Release by Means of Oxygen Consumption Measurements. *Fire and Materials*, 4:61–65, 1980.
- [14] T. Ma. Numerical Simulation of an Axi-symmetric Fire Plume: Accuracy and Limitations. Master's thesis, University of Maryland, 2001.
- [15] G. Heskestad. *SFPE Handbook*, chapter Fire Plumes. National Fire Protection Association, Quincy, Massachusetts, 2nd edition, 1995.
- [16] I.K. Puri and K. Seshadri. Extinction of Diffusion Flames Burning Diluted Methane and Diluted Propane in Diluted Air. *Combustion and Flame*, 65:137–150, 1986.
- [17] C.K. Westbrook and F.L. Dryer. Simplified Reaction Mechanisms for the Oxidation of Hydrocarbon Fuels in Flames. *Combustion Science and Technology*, 27:31–43, 1981.

- [18] R. Siegel and J. R. Howell. *Thermal Radiation Heat Transfer*. Hemisphere Publishing Corp., Philadelphia, 3 edition, 1992.
- [19] W. Grosshandler. RadCal: A Narrow Band Model for Radiation Calculations in a Combustion Environment. NIST Technical Note (TN 1402), National Institute of Standards and Technology, Gaithersburg, Maryland 20899, 1993.
- [20] G.D. Raithby and E.H. Chui. A Finite-Volume Method for Predicting Radiant Heat Transfer in Enclosures with Participating Media. *Journal of Heat Transfer*, 112(2):415–423, 1990.
- [21] J.P. Holman. *Heat Transfer*. McGraw-Hill, New York, 5th edition, 1989.
- [22] K. Prasad, C. Li, K. Kailasanath, C. Ndubizu, R. Ananth, and P.A. Tatem. Numerical modelling of methanol liquid pool fires. *Combustion Theory and Modelling*, 3:743–768, 1999.
- [23] G. Heskestad and R.G. Bill. Quantification of Thermal Responsiveness of Automatic Sprinklers Including Conduction Effects. *Fire Safety Journal*, 14:113–125, 1988.
- [24] M. DiMarzo. The Effect of Minute Water Droplets on a Simulated Sprinkler Link Thermal Response. Technical report, University of Maryland, 1999.
- [25] T.S. Chan. Measurements of Water Density and Droplet Size Distributions of Selected ESFR Sprinklers. *Journal of Fire Protection Engineering*, 6(2):79–87, 1994.
- [26] H.Z. Yu. Investigation of Spray Patterns of Selected Sprinklers with the FMRC Drop Size Measuring System. In *Fire Safety Science – Proceedings of the First International Symposium, International Association For Fire Safety Science*, pages 1165–1176, 1986.
- [27] A. Hamins and K.B. McGrattan. Reduced-Scale Experiments to Characterize the Suppression of Rack Storage Commodity Fires. Technical Report NIST Internal Report (NISTIR 6439), National Institute of Standards and Technology, Gaithersburg, Maryland 20899, 1999.
- [28] N. Cheremisinoff. *Encyclopedia of Fluid Mechanics, Volume 3: Gas-Liquid Flows*. Gulf Publishing Co., Houston, Texas, 1986.
- [29] T. Ravigururajan and M. Beltran. A Model for Attenuation of Fire Radiation Through Water Droplets. *Fire Safety Journal*, 15:171–181, 1989.
- [30] A. Tuntomo, C. Tien, and S. Park. Optical Constants of Liquid Hydrocarbon Fuels. *Combustion Science and Technology*, 84:133–140, 1992.
- [31] W. Wiscombe. Mie Scattering Calculations: Advances in Technique and Fast, Vector-Speed Computer Codes. Technical report, National Center for Atmospheric Research (NCAR), 1979.
- [32] G.M. Hale and M.R. Quarry. Optical constants of water in the 200 nm to 200 mm wavelength region. *Applied Optics*, 12:555–563, 1973.
- [33] H.Z. Yu, J.L. Lee, and H.C. Kung. Suppression of Rack-Storage Fires by Water. In *Fire Safety Science – Proceedings of the Fourth International Symposium, International Association For Fire Safety Science*, pages 901–912, 1994.
- [34] K.B. McGrattan, R.G. Rehm, and H.R. Baum. Fire-Driven Flows in Enclosures. *Journal of Computational Physics*, 110(2):285–292, 1994.

- [35] H.R. Baum, O.A. Ezekoye, K.B. McGrattan, and R.G. Rehm. Mathematical Modeling and Computer Simulation of Fire Phenomenon. *Theoretical and Computational Fluid Dynamics*, 6:125–139, 1994.
- [36] G. Continillo, F.M. Denaro, and F.S. Marra. Accuracy and Stability Analysis of Time-Integrated Schemes for Advection-Diffusion-Reaction Equations. In *Seventh International Conference on Numerical Combustion*, page 99, 1998.
- [37] J.Y. Murthy and S.R. Mathur. Radiative Heat Transfer in Axisymmetric Geometries Using an Unstructured Finite-Volume Method. *Numerical Heat Transfer, Part B*, 33:397–416, 1998.
- [38] S.H. Kim and K.Y. Huh. Assessment of The Finite-Volume Method and The Discrete Ordinate Method for Radiative Heat Transfer In a Three-Dimensional Rectangular Enclosure. *Numerical Heat Transfer, Part B*, 35:85–112, 1999.
- [39] W. Yang, T. Parker, H.D. Ladouceur, and R.J. Kee. The Interaction of Thermal Radiation and Water Mists in Fire Suppression. In *Proceedings of the Second NRIFD Symposium*. National Research Institute of Fire and Disaster (Japan), 2002.
- [40] Green Mountain Software, Boulder, Colorado. *CRAYFISHPAK User's Guide, Cray Version 1.1*, 1990.